CHAPTER 12

RADIATIVE PROPERTIES OF PARTICULATE MEDIA

12.1 INTRODUCTION

When an electromagnetic wave or a photon interacts with a medium containing small particles, the radiative intensity may be changed by absorption and/or scattering. Common examples of this interaction are sunlight being absorbed by a cloud of smoke (which is nothing but a multitude of fine particles suspended in air), scattering of sunshine by the atmosphere (the atmosphere consisting of molecules which are, in fact, tiny particles) resulting in blue skies and red sunsets, and the colors of the rainbow. Radiation scattering by particles was first dealt with by astrophysicists, who were interested in the scattering of starlight by interstellar dust. Scientists from many other disciplines are concerned with the scattering of electromagnetic waves: Meteorologists are concerned with scattering within the Earth's atmosphere (scattering of sunlight as well as scattering of radar waves for observation of precipitation); electrical engineers and physicists deal with the propagation of radio waves through the atmosphere; physicists, chemists, and engineers today use light scattering as diagnostic tools for nonintrusive and nondestructive measurements in gases, liquids, and solids. Reviews of thermal radiation phenomena in particulate media have been given by Tien and Drolen [1], and also by Dombrovsky and Baillis [2].

How much and into which direction a particle scatters an electromagnetic wave passing through its vicinity depends on (*i*) the shape of the particle, (*ii*) the material of the particle (i.e., the complex index of refraction, $m = n - ik$), (*iii*) its relative size, and (*iv*) the clearance between particles. In radiative analyses the shape of particles is usually assumed to be spherical (for spherical and irregularly shaped objects) or cylindrical (for long fibrous materials). These simplifying assumptions give generally excellent results, since averaging over many millions of irregular shapes tends to smoothen the irregularities [1]. In the following discussion we shall primarily consider absorption and scattering by spherical particles, as shown in Fig. 12-1.

An electromagnetic wave or photon passing through the immediate vicinity of spherical particles will be absorbed or scattered. The scattering is due to three separate phenomena, namely, (*i*) diffraction (waves never come into contact with the particle, but their direction of propagation is altered by the presence of the particle), (*ii*) reflection by a particle (waves reflected from the surface of the sphere), and (*iii*) refraction in a particle (waves that penetrate into the sphere and, after partial absorption, reemerge traveling into a different direction). The vast majority of photons are scattered elastically, i.e., their wavelength (and energy) remain unchanged. A tiny fraction undergo *inelastic* or *Raman scattering* (the photons reemerge with a different wavelength). While very important for optical diagnostics, the *Raman effect* is unimportant for the

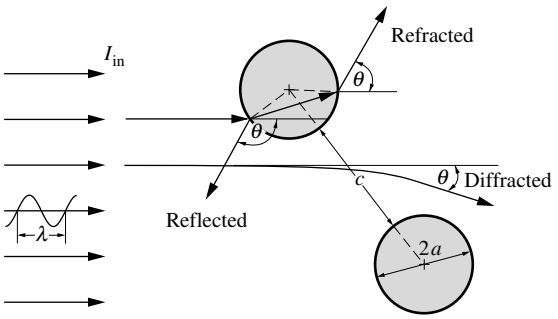

FIGURE 12-1
Interaction between electromagnetic waves and spherical particles.

evaluation of radiative heat transfer rates, and we shall treat only elastic scattering in this book. If scattering by one particle is not affected by the presence of surrounding particles, we speak of *independent scattering*, otherwise we have *dependent scattering*. Thus, the radiative properties of a cloud of spherical particles of radius a, interacting with an electromagnetic wave of wavelength λ, are governed by three independent nondimensional parameters:

$$\text{complex index of refraction:} \quad m = n - ik, \tag{12.1}$$

$$\text{size parameter:} \quad x = 2\pi a/\lambda, \tag{12.2}$$

$$\text{clearance-to-wavelength ratio:} \quad c/\lambda. \tag{12.3}$$

If scattering is independent ($c/\lambda \gg 1$), then only the first two parameters are needed. For the classification of dependent scattering, the clearance-to-wavelength ratio is often replaced by a purely geometric parameter, c/a, which in turn may be related to the volume fraction of particles, f_v. While in earlier works, for example that by van de Hulst [3], it was assumed that dependent effects were a function of particle separation only, it is now known that wavelength effects also play a role. This was first recognized by Hottel and coworkers [4]. Since then, a number of investigators, notably Tien and coworkers [1, 5–9], have established limits for when dependent effects must be considered. Their results, summarized in Fig. 12-2, show that dependent scattering effects may be ignored as long as $f_v < 0.006$ or $c/\lambda > 0.5$. Since these values include nearly all heat transfer applications, only independent scattering is discussed in the present chapter. The reader interested in the prediction of dependent scattering properties should consult the monograph by Tien and Drolen [1].

12.2 ABSORPTION AND SCATTERING FROM A SINGLE SPHERE

The scattering and absorption of radiation by single spheres was first discussed during the later part of the nineteenth century by Lord Rayleigh [10, 11], who obtained a simple solution for spheres whose diameters are much smaller than the wavelength of radiation (small size parameter, $x \ll 1$). This work was followed in the 1890s by the work of Lorenz* [12, 13], in 1908 by the classical paper of Gustav Mie† [14], and in 1909 by a similar treatment of Debye [15].

*__Ludvig Lorenz (1829–1991)__
Danish mathematician and physicist. Lorenz studied at the Technical University of Copenhagen and, starting in 1876, he served as professor of physics at the Military Academy in Copenhagen. He also independently, and around the time as Hendrik Anton Lorentz (see p. 58), discovered the relationship between the refractive index and the density of a medium, generally known as the Lorenz-Lorentz formula.

†__Gustav Mie (1868–1957)__
German physicist. After studying at the universities of Rostock and Heidelberg, he served as professor of physics at various German universities.

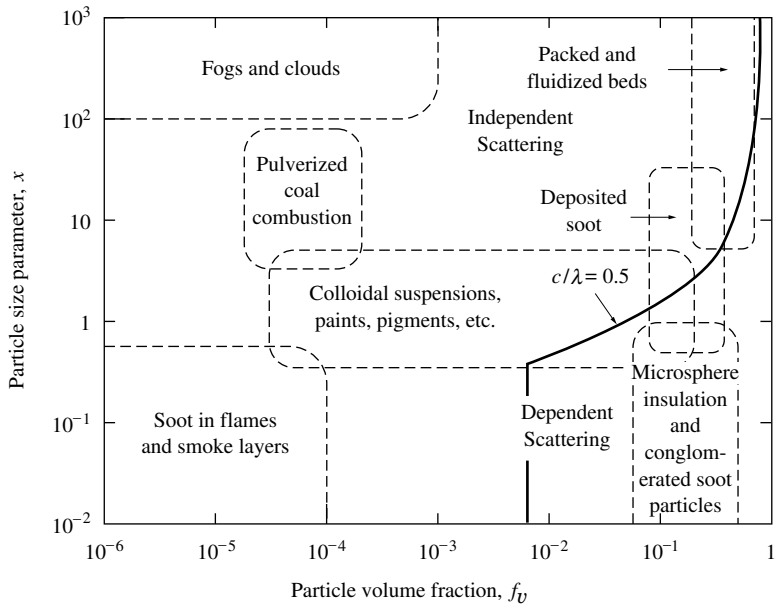

FIGURE 12-2
Scattering regime map for independent and dependent scattering [1].

Lorenz's work was based on his own theory of electromagnetism rather than Maxwell's, while Mie developed an equivalent solution to Maxwell's equations [cf. equations (2.11) through (2.14)] for an electromagnetic wave train traveling through a medium with an imbedded sphere. Although the work of Lorenz predates that of Mie, the general theory describing radiative scattering by absorbing spheres is generally referred to as the "Mie theory." More recently, in recognition of Lorenz's contributions, the terminology "Lorenz–Mie theory" has also become popular. An exhaustive review of the history of the development of particle scattering theory has been given by Kerker [16].

The complicated *Lorenz–Mie scattering theory* must generally be used if the size of the sphere is such that it is too large to apply the Rayleigh theory, but too small to employ geometric optics (which requires $x \gg 1$ as well as $kx \gg 1$). We shall give here a very brief discussion of the Lorenz–Mie theory and some representative results. Detailed derivations may be found in the books on the subject by van de Hulst [3], Kerker [16], Deirmendjian [17], and Bohren and Huffman [18].

The amount of scattering and absorption by a particle is usually expressed in terms of the *scattering cross-section*, C_{sca}, and *absorption cross-section*, C_{abs}. The total amount of absorption and scattering, or extinction, is expressed in terms of the *extinction cross-section*,

$$C_{ext} = C_{abs} + C_{sca}. \tag{12.4}$$

Often *efficiency factors* Q are used instead of cross-sections; they are nondimensionalized with the projected surface area of the sphere, or

$$\textit{absorption efficiency factor:} \quad Q_{abs} = \frac{C_{abs}}{\pi a^2}, \tag{12.5}$$

$$\textit{scattering efficiency factor:} \quad Q_{sca} = \frac{C_{sca}}{\pi a^2}, \tag{12.6}$$

$$\textit{extinction efficiency factor:} \quad Q_{ext} = \frac{C_{ext}}{\pi a^2}, \tag{12.7}$$

and

$$Q_{\text{ext}} = Q_{\text{abs}} + Q_{\text{sca}}. \tag{12.8}$$

Radiation interacting with a spherical particle may be scattered away from its original direction by an angle Θ, i.e., the propagation vector of the electric and magnetic fields may be redirected by the scattering angle (Fig. 12-1). This deflection from the incident direction is described by the angle Θ alone because, for a spherical particle, there can be no azimuthal variation. The intensity of the wave scattered by the angle Θ [i.e., the magnitude of the Poynting vector, equation (2.42)] is proportional to two complex *amplitude functions* $S_1(\Theta)$ and $S_2(\Theta)$, where the subscripts denote two perpendicular polarizations. Once these amplitude functions have been determined, the intensity of radiation I_{sca}, scattered by an angle Θ from the incident unpolarized beam of strength I_{in}, may be calculated [3, 16, 17] from

$$\frac{I_{\text{sca}}(\Theta)}{I_{\text{in}}} = \frac{1}{2}\frac{i_1 + i_2}{x^2}, \tag{12.9}$$

where i_1 and i_2 are the nondimensional polarized intensities calculated from

$$i_1(x, m, \Theta) = |S_1|^2, \quad i_2(x, m, \Theta) = |S_2|^2. \tag{12.10}$$

From equation (12.9) it follows that the total amount of energy scattered by one sphere into all directions [3] is

$$Q_{\text{sca}} = \frac{C_{\text{sca}}}{\pi a^2} = \frac{a^2}{\pi a^2}\int_{4\pi}\frac{I_{\text{sca}}}{I_{\text{in}}}\,d\Omega = \frac{1}{x^2}\int_0^{\pi}(i_1 + i_2)\,\sin\Theta\,d\Theta. \tag{12.11}$$

The fraction of this energy that is scattered into any given direction is denoted by the *scattering phase function* $\Phi(\Theta)$, which is normalized such that

$$\frac{1}{4\pi}\int_{4\pi}\Phi(\hat{\mathbf{s}}_i, \hat{\mathbf{s}})\,d\Omega \equiv 1. \tag{12.12}$$

Thus, together with equation (12.9), the scattering phase function may be expressed as

$$\Phi(\Theta) = \frac{i_1 + i_2}{\dfrac{1}{4\pi}\displaystyle\int_{4\pi}(i_1 + i_2)\,d\Omega} = 2\frac{i_1 + i_2}{x^2 Q_{\text{sca}}}. \tag{12.13}$$

Finally, total extinction by a single particle (absorption within the particle, plus scattering into all directions) is related to the real part of the amplitude functions by

$$Q_{\text{ext}} = \frac{4}{x^2}\,\Re\{S(0)\}, \tag{12.14}$$

where the amplitude function S is without a subscript because $S_1(0) = S_2(0)$.

The major difficulty in the evaluation of scattering properties lies in the calculation of the complex amplitude functions $S_1(\Theta)$ and $S_2(\Theta)$. For the general case of arbitrary values for the complex index of refraction m and the size parameter x, the full Lorenz–Mie equations as expressed by van de Hulst [3] must be employed,

$$S_1(\Theta) = \sum_{n=1}^{\infty}\frac{2n+1}{n(n+1)}\left[a_n\pi_n(\cos\Theta) + b_n\tau_n(\cos\Theta)\right], \tag{12.15}$$

$$S_2(\Theta) = \sum_{n=1}^{\infty}\frac{2n+1}{n(n+1)}\left[b_n\pi_n(\cos\Theta) + a_n\tau_n(\cos\Theta)\right], \tag{12.16}$$

where the direction-dependent functions π_n and τ_n are related to Legendre polynomials P_n (for a description of these polynomials, see, e.g., Wylie [19]) by

$$\pi_n(\cos\Theta) = \frac{dP_n(\cos\Theta)}{d\cos\Theta}, \tag{12.17}$$

$$\tau_n(\cos\Theta) = \cos\Theta\,\pi_n(\cos\Theta) - \sin^2\Theta\,\frac{d\pi_n(\cos\Theta)}{d\cos\Theta}, \tag{12.18}$$

and the Mie scattering coefficients a_n and b_n are complex functions of x and $y = mx$,

$$a_n = \frac{\psi_n'(y)\psi_n(x) - m\psi_n(y)\psi_n'(x)}{\psi_n'(y)\zeta_n(x) - m\psi_n(y)\zeta_n'(x)}, \tag{12.19}$$

$$b_n = \frac{m\psi_n'(y)\psi_n(x) - \psi_n(y)\psi_n'(x)}{m\psi_n'(y)\zeta_n(x) - \psi_n(y)\zeta_n'(x)}. \tag{12.20}$$

The functions ψ_n and ζ_n are known as *Riccati–Bessel functions*, and are related to Bessel and Hankel functions [19,20] by

$$\psi_n(z) = \left(\frac{\pi z}{2}\right)^{1/2} J_{n+1/2}(z), \quad \zeta_n(z) = \left(\frac{\pi z}{2}\right)^{1/2} H_{n+1/2}(z). \tag{12.21}$$

Equations (12.15) and (12.16) may be substituted into equations (12.11) and (12.14). Using the fact that—like Legendre polynomials—the functions π_n and τ_n constitute sets of orthogonal functions leads to

$$Q_{\text{sca}} = \frac{2}{x^2}\sum_{n=1}^{\infty}(2n+1)(|a_n|^2 + |b_n|^2), \tag{12.22}$$

$$Q_{\text{ext}} = \frac{2}{x^2}\sum_{n=1}^{\infty}(2n+1)\Re\{a_n + b_n\}. \tag{12.23}$$

Once all Mie scattering coefficients a_n and b_n have been determined, the phase function Φ may also be evaluated from equation (12.13), but this calculation tends to be extremely tedious because of the nature of equation (12.10), and because the calculations must be carried out anew for every scattering angle Θ. To facilitate the calculations Chu and Churchill [21,22] expressed the scattering phase function as a series in Legendre polynomials,

$$\Phi(\Theta) = 1 + \sum_{n=1}^{\infty} A_n P_n(\cos\Theta), \tag{12.24}$$

where the coefficients A_n are directly related to the Mie scattering coefficients a_n and b_n through some rather complicated formulae not reproduced here. The great advantage of this formulation is that, once the A_n have been determined, the value of the phase function Φ is determined quickly for any or all scattering directions.

In many applications the use of the complicated scattering phase function described by equation (12.24) is too involved. For a simpler analysis the directional scattering behavior may be described by the average cosine of the scattering angle, known as the *asymmetry factor*, and related to the phase function by

$$g = \overline{\cos\Theta} = \frac{1}{4\pi}\int_{4\pi}\Phi(\Theta)\cos\Theta\,d\Omega. \tag{12.25}$$

For the case of *isotropic scattering* (i.e., equal amounts are scattered into all directions, and $\Phi \equiv 1$) the asymmetry factor vanishes; g also vanishes if scattering is symmetrical about the plane

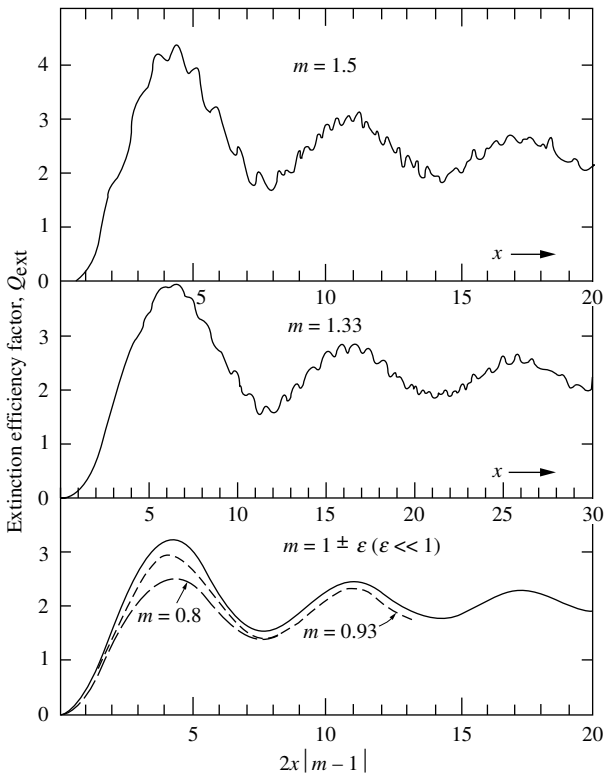

FIGURE 12-3
Extinction efficiency factors for dielectric spheres for several refractive indices [3].

perpendicular to beam propagation. If the particle scatters more radiation into the forward directions ($\Theta < \pi/2$), g is positive; if more radiation is scattered into the backward direction ($\Theta > \pi/2$), g is negative. For spherical particles the asymmetry factor is readily calculated [18] as

$$g = \overline{\cos\Theta} = \frac{4}{x^2 Q_{sca}} \sum_{n=1}^{\infty} \left[\frac{n(n+2)}{n+1} \Re\{a_n a_{n+1}^* + b_n b_{n+1}^*\} + \frac{2n+1}{n(n+1)} \Re\{a_n b_n^*\} \right]. \tag{12.26}$$

The calculation of the scattering Mie coefficients a_n and b_n is no trivial matter even in these days of supercomputers: The relationships leading to their determination are involved and require the frequent evaluation of complicated functions with complex arguments. For large size parameters x many terms need to be calculated ($n_{max} \approx 2x$). Recursion formulae for the functions π_n, τ_n, ψ_n, and ζ_n have been given by Deirmendjian [17] and others, which evaluate these functions for increasing values of n in terms of previously calculated functions. Deirmendjian observed that the accuracy of calculations decreases for increasing n, causing complete failure of the calculations for large values of the size parameter x (for which many terms are required in the series for the amplitude functions), even if double-precision arithmetic is employed. This problem was overcome by Kattawar and Plass [23] who showed that all four functions may be reduced to functions each belonging to one of two sets: One set has stable recursion formulae for increasing n (i.e., round-off error *decreases* with growing n), and the other set is stable for decreasing values of n (setting the function to zero for a larger n than required in the series results in very accurate values for slightly smaller n). Wiscombe [24] compared the accuracy and stability of several Lorenz–Mie scattering computer solution routines and discussed the efficiency of different calculation methods (whether to use upward or downward recursion, what recursion formulae to use, etc.). Some representative results of Lorenz–Mie calculations are shown in Figs. 12-3 through 12-5. Figure 12-3 shows typical behavior of efficiency factors, demonstrated with the extinction efficiency of a dielectric ($k \equiv 0$) for a number of different

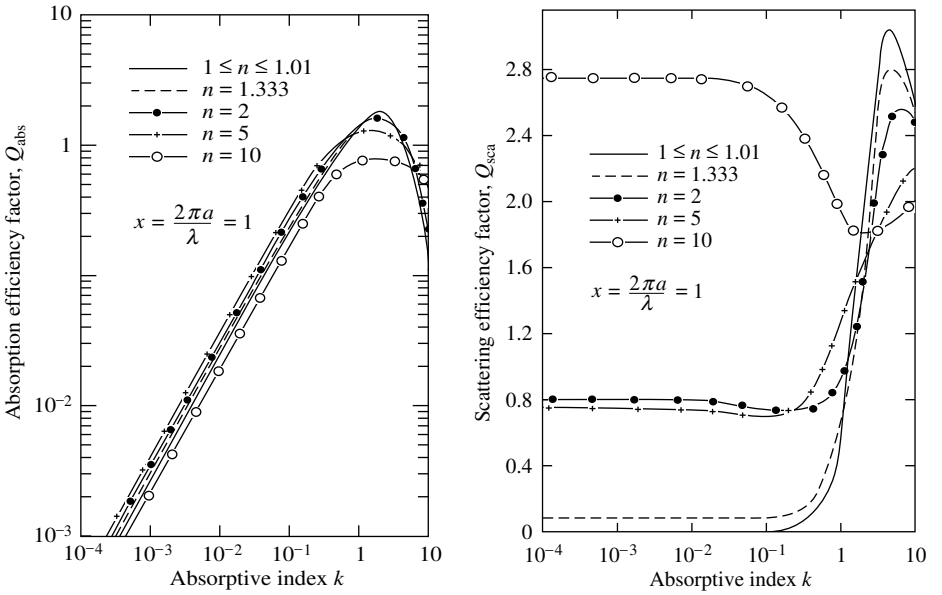

FIGURE 12-4
Efficiency factors as functions of complex index of refraction, $m = n - ik$, for a size parameter of $x = 1$ [23]: *(a)* absorption efficiency factor, *(b)* scattering efficiency factor.

refractive indices n. Observe that there is a primary oscillation in the variation of Q_{ext} with size parameter, upon which secondary oscillations are superimposed (stronger for larger refractive indices). Note also that the oscillations become smaller for larger size parameters, and $Q_{ext} \to 2$ as $x \to \infty$ (for dielectrics as well as metals). Figure 12-4 shows the qualitative behavior of efficiency factors for absorption, Q_{abs}, and scattering, Q_{sca}, respectively, for a fixed value of the size parameter ($x = 1$), as a function of absorptive index k. The absorption efficiency factors may vary by many orders of magnitude over the range of absorptive index k, while the scattering efficiency remains constant over great changes of k. Finally, Fig. 12-5 shows some representative scattering phase functions, $\Phi(\Theta)$. Figure 12-5*a* shows the scattering behavior of very small particles (known as *Rayleigh scattering*): The scattering is symmetric to the plane perpendicular to the incident beam, and is nearly isotropic with slight forward- and backward-scattering peaks and somewhat lesser scattering to the sides. Figure 12-5*b* demonstrates the behavior of particles with refractive indices close to unity (known as *Rayleigh–Gans scattering*): Nearly all of the scattered energy is scattered into forward directions with some scattering into a few preferred other directions. This behavior becomes more extreme as the size parameter increases. Figure 12-5*c* shows the phase function of a typical dielectric: The scattering has a strong forward component; otherwise the scattering behavior demonstrates rapid maxima and minima at varying scattering angles, with much stronger amplitudes than for *Rayleigh–Gans scattering* (note the change in scale). The variations are not quite so extreme as in Fig. 12-5*b* owing to the large value for n. The behavior of a typical metal (aluminum at 3.1 μm) is shown in Fig. 12-5*d*: Besides a strong forward-scattering peak these particles display lesser-degree oscillations than dielectrics. These phase functions have been calculated with the author's own code, `mmmie`, which is included in Appendix F for the convenience of the reader.

12.3 RADIATIVE PROPERTIES OF A PARTICLE CLOUD

In all problems of radiative heat transfer with particulate scattering and absorption, we have to deal with a large collection of particles. If the scattering is independent, as is assumed in this

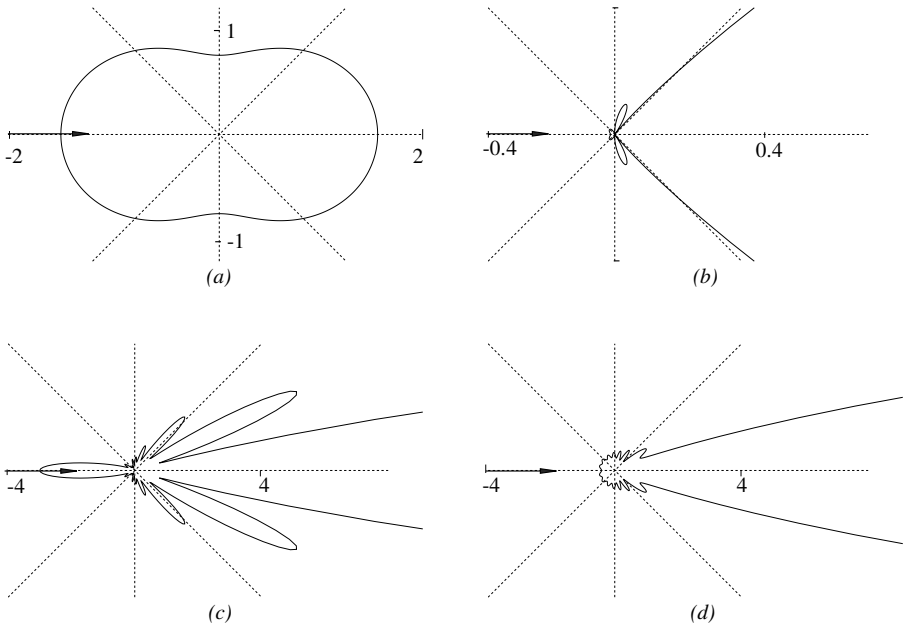

FIGURE 12-5
Polar plot of scattering phase functions for single spherical particles: (*a*) small sphere with $x = 0.001$; (*b*) dielectric with $x = 5$ and $m = 1.0001$; (*c*) dielectric sphere with $x = 10$ and $m = 2$; and (*d*) metallic sphere (aluminum) with $x = 10$ and $m = 4.46 - 31.5i$.

chapter, then the effects of large numbers of particles are simply additive. For simplicity, it is often assumed that particle clouds consist of spheres that are all equally large. More accurate analyses take into account that particles of many different sizes may occur within a single cloud, and that these sizes often vary by orders of magnitude. We shall briefly describe both approaches in the following paragraphs.

Clouds of Uniform Size Particles

The fraction of energy scattered by all particles per unit length along the direction of the incoming beam is called the *scattering coefficient* [as defined by equation (10.6)] and is equal to the scattering cross-section summed over all particles. If N_T is the number of particles per unit volume, all of uniform radius a, then

$$\sigma_{s\lambda} = N_T C_{\text{sca}} = \pi a^2 N_T Q_{\text{sca}}, \tag{12.27}$$

and, similarly, for absorption and extinction,

$$\kappa_\lambda = N_T C_{\text{abs}} = \pi a^2 N_T Q_{\text{abs}}, \tag{12.28}$$

$$\beta_\lambda = \kappa_\lambda + \sigma_{s\lambda} = N_T C_{\text{ext}} = \pi a^2 N_T Q_{\text{ext}}. \tag{12.29}$$

Since the scattering phase function (or the directional distribution of scattered energy) in a cloud of uniform particles is the same for each particle, it is also the same for the particle cloud, or

$$\Phi_{T\lambda}(\Theta) = \Phi(\Theta), \tag{12.30}$$

and similarly for the asymmetry factor,

$$g_{T\lambda} = \overline{(\cos\Theta)}_{T\lambda} = \overline{\cos\Theta}. \tag{12.31}$$

In both cases we have temporarily added the subscript T (to distinguish the total cloud of particles from a single particle) and λ to emphasize the fact that both quantities are spectral quantities that may vary with wavelength.

If total (i.e., spectrally integrated) properties are desired, equations (12.27) through (12.29) may be integrated to obtain Planck-mean or Rosseland-mean coefficients (for absorption, scattering, and/or extinction), as defined by equations (11.182) and (11.188), or

$$y_P = \frac{\pi}{\sigma T^4} \int_0^\infty I_{b\lambda}\, y_\lambda \, d\lambda, \qquad y = \kappa,\ \sigma_s,\ \text{or } \beta, \tag{12.32}$$

$$\frac{1}{y_R} = \frac{\pi}{4\sigma T^3} \int_0^\infty \frac{1}{y_\lambda} \frac{dI_{b\lambda}}{dT} d\lambda, \qquad y = \kappa,\ \sigma_s,\ \text{or } \beta. \tag{12.33}$$

Similarly, total emissivities and absorptivities may be obtained from equation (11.171). Since the efficiency factors Q may vary rapidly across the spectrum, these integrations generally need to be done numerically.

Clouds of Nonuniform Size Particles

For clouds of particles of nonuniform size it is customary to describe the number of particles as a function of radius in the form of a *particle distribution function*. A number of different forms for the distribution function have been used by various researchers. We introduce here the so-called *modified gamma distribution* [17],

$$n(a) = Aa^\gamma \exp(-Ba^\delta), \quad 0 \le a < \infty, \tag{12.34}$$

which vanishes at $a = 0$ and $a \to \infty$. This distribution function reduces to the *gamma distribution* if $\delta = 1$. The four constants A, B, γ, and δ are positive and real, and γ and δ are usually chosen to be integers. They must be determined from measurable quantities such as total number of particles (per unit volume),

$$N_T = \int_0^\infty n(a)\, da = A \int_0^\infty a^\gamma \exp(-Ba^\delta)\, da = \frac{A\Gamma\left(\frac{\gamma+1}{\delta}\right)}{\delta B^{(\gamma+1)/\delta}}. \tag{12.35}$$

Here Γ is the *gamma function*,

$$\Gamma(z) = \int_0^\infty e^{-t} t^{z-1}\, dt, \tag{12.36}$$

and has been tabulated, e.g., by Abramowitz and Stegun [20]. Equation (12.35) shows that the constant A is essentially given by N_T. The total volume of particles per unit volume, or *volume fraction*, is given by

$$f_v = \int_0^\infty \tfrac{4}{3}\pi a^3 n(a)\, da = \frac{4\pi A\Gamma\left(\frac{\gamma+4}{\delta}\right)}{3\delta B^{(\gamma+4)/\delta}}. \tag{12.37}$$

Assuming that all particles have the same optical properties, we may again determine the scattering coefficient for a particle cloud by adding the scattering cross-section over all particles but, because of the particle size distribution, this is now an integral rather than a simple sum,

$$\sigma_{s\lambda} = \int_0^\infty C_{\text{sca}} n(a)\, da = \pi \int_0^\infty Q_{\text{sca}} a^2 n(a)\, da, \tag{12.38}$$

and, similarly, for absorption and extinction,

$$\kappa_\lambda = \int_0^\infty C_{\text{abs}} n(a)\, da = \pi \int_0^\infty Q_{\text{abs}} a^2 n(a)\, da, \tag{12.39}$$

$$\beta_\lambda = \int_0^\infty C_{\text{ext}} n(a)\, da = \pi \int_0^\infty Q_{\text{ext}} a^2 n(a)\, da. \tag{12.40}$$

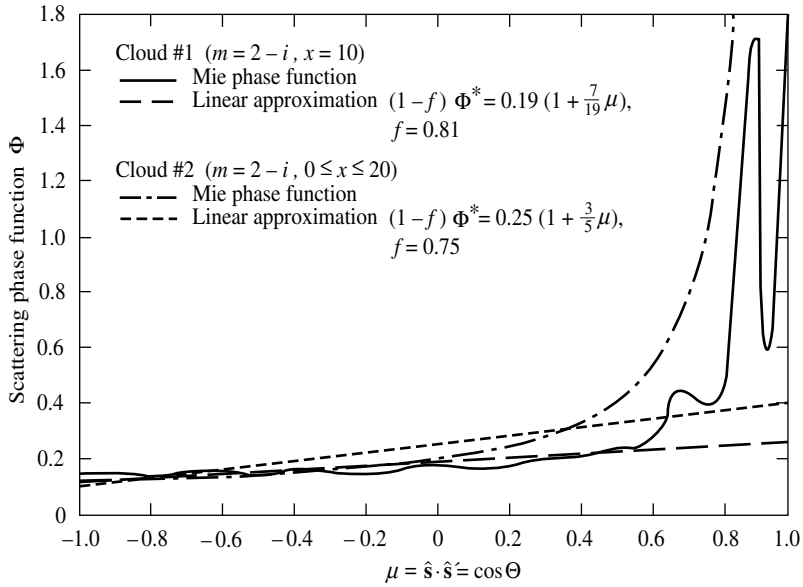

FIGURE 12-6
Lorenz–Mie scattering phase function for clouds of absorbing particles [25].

For nonuniform particles the scattering phase function is not the same for all particles. From the definition of the phase function, it follows that the scattered energies into a given direction must be summed over all particles and then normalized, or

$$\Phi_{T\lambda}(\Theta) = \frac{\displaystyle\int_0^\infty (i_1 + i_2)\, n(a)\, da}{\displaystyle\frac{1}{4\pi}\int_{4\pi}\left[\int_0^\infty (i_1 + i_2)\, n(a)\, da\right] d\Omega} = \frac{\displaystyle\int_0^\infty C_{\text{sca}}(a)\,\Phi(a,\Theta)\, n(a)\, da}{\displaystyle\int_0^\infty C_{\text{sca}}(a)\, n(a)\, da}$$

$$= \frac{1}{\sigma_{s\lambda}}\int_0^\infty C_{\text{sca}}(a)\,\Phi(a,\Theta)\, n(a)\, da, \tag{12.41}$$

and, similarly,

$$g_{T\lambda} = \overline{(\cos\Theta)}_{T\lambda} = \frac{1}{\sigma_{s\lambda}}\int_0^\infty C_{\text{sca}}(a)\, g(a)\, n(a)\, da. \tag{12.42}$$

Again, if total properties are needed, equations (12.38) through (12.40) may be integrated over the entire spectrum.

Figures 12-6 and 12-7 show a few typical scattering phase functions for absorbing and nonabsorbing particle clouds, calculated with program `mmmie` of Appendix F. Two types of particles are considered, one nonabsorbing with an index of refraction $m = 2$, the other one absorbing with $m = 2 - i$. The particles are either in clouds of constant radius $a = 5\,\mu$m, or in clouds with a distribution function

$$n(a) = 27{,}230a^2 \exp(-1.7594a), \tag{12.43}$$

which has its maximum at $a = 5\,\mu$m. All the particle clouds have a number density of 10^4 particles/cm^3, and the Lorenz–Mie calculations have been carried out for a typical wavelength of $\lambda = 3.1416\,\mu$m, resulting in a size parameter of $x = 2\pi a/\lambda = 10$ for the constant-radius clouds, and a range of significant size parameters of $0 < x \le 20$ for clouds with particle size distribution. The radiative properties for the four different particle clouds are summarized in Table 12.1. Absorption and scattering coefficients for constant-radius and particle distribution

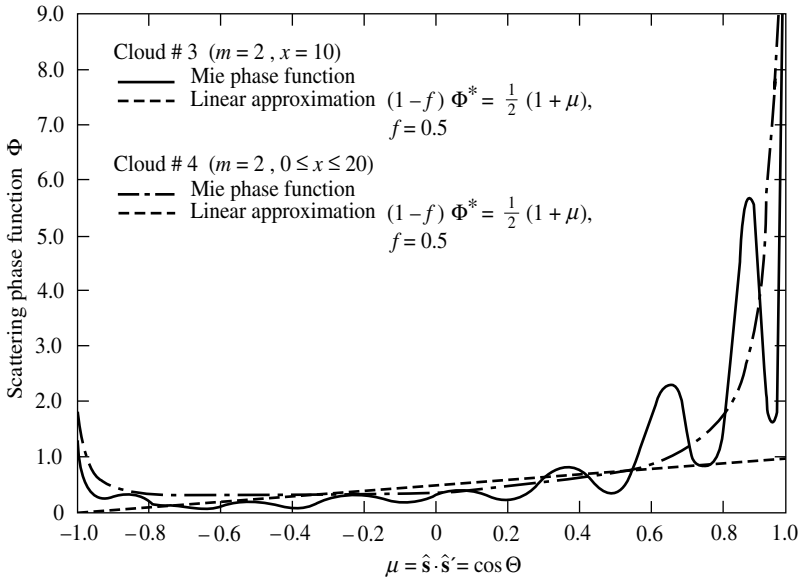

FIGURE 12-7
Lorenz–Mie scattering phase function for clouds of dielectric particles [25].

TABLE 12.1
Radiative properties of typical particle clouds ($N_T = 10^4/\text{cm}^3$, $\lambda = 3.1416\,\mu\text{m}$).

	Cloud#1 Const. Radius $a = 5\,\mu$m $m = 2 - i$	Cloud#2 Size Distr. $n(a)$ $m = 2 - i$	Cloud#3 Const. Radius $a = 5\,\mu$m $m = 2$	Cloud#4 Size Distr. $n(a)$ $m = 2$
Absorption coefficient κ [cm^{-1}]	8.307×10^{-3}	1.524×10^{-3}	0	0
Scattering coefficient σ_s [cm^{-1}]	1.073×10^{-2}	1.674×10^{-3}	6.420×10^{-2}	3.363×10^{-3}
Extinction coefficient β [cm^{-1}]	1.904×10^{-2}	3.198×10^{-3}	6.420×10^{-2}	3.363×10^{-3}
Scattering albedo	0.5634	0.5235	1	1
Terms needed for phase function	26	35	27	33

clouds differ considerably, primarily because the average particle size in equation (12.43) is less than 5 μm, being 2.33 μm for the volume- or mass-averaged radius, and 1.52 μm for the number-averaged radius. Observe that the phase functions for uniform particle size clouds display strong oscillations due to diffraction peaks, because the phase function is identical to the one of single particles (cf. Fig. 12-5). Since the diffraction peaks shift slightly with changing size parameters, these peaks and valleys are smoothed out for clouds with varying particle sizes. For these types of clouds the phase function becomes very smooth with only a strong forward-scattering peak remaining (plus a weaker backward-scattering peak for dielectric particles). Thus, the analysis of scattering phenomena may actually be simpler if there is a particle size distribution! Figures 12-6 and 12-7 also shows linear anisotropic approximations to these phase functions, as discussed in Section 12.9.

Bohren and Huffman [18] have shown that this smoothing effect occurs for the efficiency factors as well as for the phase function, requiring only a small deviation from uniform-size parti-

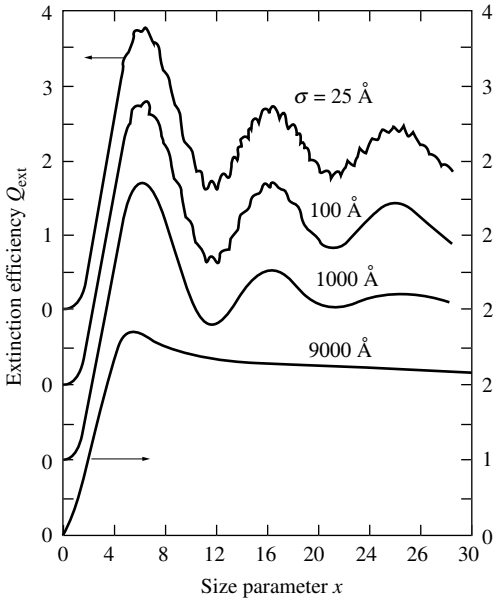

FIGURE 12-8
The effect of size dispersion on the extinction efficiency for water droplets and visible light (σ = standard deviation in Gaussian distribution function) [18].

cles to be present. Figure 12-8 shows the extinction efficiency for clouds of water droplets, which are assumed to have a Gaussian distribution function centered around a mean particle size with standard deviation σ. Small deviations from uniform size blur out the high-frequency variation (called the *ripple structure*), while slightly larger deviations also dampen out the low-frequency variations of the extinction efficiency (called the *interference structure*). Similar smoothing effects occur in a cloud of uniform-size particles of irregular shape as shown by Hodkinson [26] for aqueous suspensions of irregular quartz particles.

12.4 RADIATIVE PROPERTIES OF SMALL SPHERES (RAYLEIGH SCATTERING)

Radiative scattering by spheres that are small compared with wavelength was first described by Lord Rayleigh [10, 11] long before the development of Mie's theory [14]. However, results for small particles are here most easily obtained by taking the appropriate limits in the general solution to Mie's equations.

If the scattering particles are extremely small, then the size parameter $x = 2\pi a/\lambda$ becomes very small. Such behavior is primarily observed with gas molecules (which are, in fact, very tiny particles). There are, however, also some multimolecule solid particles that fall into the Rayleigh scattering regime, e.g., soot particles (whose diameters are often smaller than 10 nm and which, in combustion applications, are irradiated by light of approximately 3 μm, resulting in $x \approx 0.01$).

In the limit of $x \to 0$ it is relatively straightforward to show that only the a_1 in equations (12.19) and (12.20) is nonzero, or

$$S_2(\Theta) = S_1(\Theta)\cos\Theta = i\frac{m^2-1}{m^2+2}x^3\cos\Theta, \tag{12.44}$$

that is, the amplitude function for one polarization is independent of scattering angle Θ. Substitution into equations (12.11) and (12.14) then gives the efficiency factors as

$$Q_{sca} = \frac{8}{3}\left|\frac{m^2-1}{m^2+2}\right|^2 x^4, \tag{12.45}$$

$$Q_{abs} = -4\Im\left\{\frac{m^2-1}{m^2+2}\right\}x \approx Q_{ext}, \tag{12.46}$$

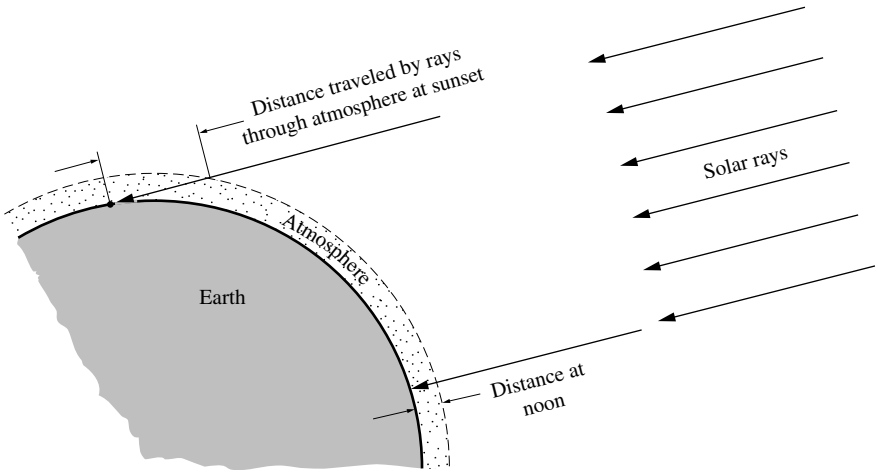

FIGURE 12-9
Distance traveled through Earth's atmosphere by solar rays.

where the last equality in equation (12.46) is due to the fact that $x^4 \ll x$, so that scattering may be neglected as compared with absorption. We observe the wavelength dependence of the scattering efficiency to be

$$Q_{\text{sca}} \propto \frac{1}{\lambda^4} \propto \nu^4. \tag{12.47}$$

We note in passing that this fact explains the colors of the sky: During most of the day, when the sun's rays travel a relatively short distance through Earth's atmosphere (cf. Fig. 12-9), only the shortest wavelengths are scattered away in any appreciable amounts from the sun's direct path; they are scattered again and again by the molecules in the atmosphere, providing us with a blue sky (blue light having the shortest wavelength within the visible spectrum). Close to sunset, however, the sun's rays travel at a grazing angle through the atmosphere to the observer, so that all but the very longest wavelengths (of the visible spectrum) have been scattered away from the direct path, giving the sun a red appearance. Without the atmosphere the sky would appear black to us, as witnessed by the astronauts visiting the (atmosphere-less) moon.

The wavelength dependence of the absorption efficiency, on the other hand, is

$$Q_{\text{abs}} \propto \frac{1}{\lambda} \propto \nu, \tag{12.48}$$

which describes the spectral behavior of small particles such as soot reasonably well.

The phase function for Rayleigh scattering follows from equations (12.44) and (12.13) as

$$\Phi(\Theta) = \tfrac{3}{4}(1 + \cos^2\Theta), \tag{12.49}$$

where the two terms are the contributions from the two perpendicular polarizations, as shown in Fig. 12-10. It is observed that the phase function is symmetric as far as forward and backward scattering is concerned, and does not deviate too strongly from isotropic scattering.

The absorption coefficient for a cloud of nonuniform-size small particles follows from equations (12.39) and (12.46) as

$$\kappa_\lambda = \pi \int_0^\infty Q_{\text{abs}} a^2 n(a)\, da = -4\Im\left\{\frac{m^2-1}{m^2+2}\right\} \int_0^\infty \left(\frac{2\pi a}{\lambda}\right) \pi a^2 n(a)\, da. \tag{12.50}$$

The integral in this equation may be related to the *volume fraction* f_v,

$$f_v = \int_0^\infty \left(\frac{4}{3}\pi a^3\right) n(a)\, da, \tag{12.51}$$

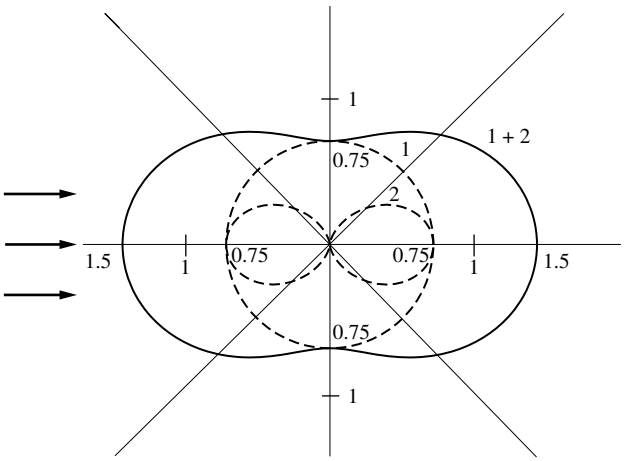

FIGURE 12-10
Polar diagram of Rayleigh phase function: 1, polarized with electric vector in plane perpendicular to paper; 2, polarized in plane of paper; 1+2, unpolarized.

so that the absorption coefficient for small particles reduces to

$$\kappa_\lambda = -\mathfrak{I}\left\{\frac{m^2-1}{m^2+2}\right\}\frac{6\pi f_v}{\lambda}, \tag{12.52}$$

or, expanding the complex index of refraction, $m = n - ik$,

$$\kappa_\lambda = \frac{36\pi nk}{(n^2-k^2+2)^2+4n^2k^2}\frac{f_v}{\lambda}. \tag{12.53}$$

Therefore, for particles small enough that Rayleigh scattering holds, the absorption coefficient does not depend on particle size distribution, but only on the total volume occupied by all particles (per unit system volume).

Example 12.1. During the burning of propane it is observed that the products contain a volume fraction of $10^{-4}\%$ of soot with complex index of refraction $m = 2.21 - 1.23i$ (measured at a wavelength of $3\,\mu$m). Assuming a mean particle diameter of $0.05\,\mu$m, determine the absorption and scattering efficiency of this soot cloud as well as its absorption coefficient, all at a wavelength of $3\,\mu$m.

Solution
For the given diameter and wavelength the particle size parameter is $x = \pi \times 0.05\,\mu\text{m}/3\,\mu\text{m} = 0.0524 \ll 1$ and we assume Rayleigh scattering to hold for all particles. For all three properties we need to evaluate the complex ratio $(m^2-1)/(m^2+2)$:

$$\begin{aligned}\frac{m^2-1}{m^2+2} &= \frac{2.21^2 - 2\times 2.21\times 1.23i - 1.23^2 - 1}{2.21^2 - 2\times 2.21\times 1.23i - 1.23^2 + 2}\\ &= \frac{2.3712 - 5.4366i}{5.3712 - 5.4366i}\times\frac{5.3712 + 5.4366i}{5.3712 + 5.4366i}\\ &= \frac{42.2928 - 16.3098i}{58.4064} = 0.7241 - 0.2792i.\end{aligned}$$

Thus, the efficiencies can be evaluated as

$$Q_{\text{sca}} = \frac{8}{3}|0.7241 - 0.2792i|^2 \times (0.0524)^4 = 1.21\times 10^{-5},$$

and

$$Q_{\text{abs}} = -4\times(-0.2792)\times 0.0524 = 5.85\times 10^{-2},$$

showing that scattering may indeed be neglected compared with absorption. The absorption coefficient follows from equation (12.53) as

$$\kappa_\lambda = -(-0.2792)\times\frac{6\pi\times 10^{-4}/100}{3\times 10^{-4}\,\text{cm}} = 0.01754\,\text{cm}^{-1},$$

that is, any radiation (at 3 μm) penetrating into such a soot cloud would be attenuated to $1/e$ of its original intensity over a distance of $1/\kappa_\lambda = 57$ cm.

12.5 RAYLEIGH–GANS SCATTERING

A near-dielectric sphere with $k \approx 0$ and with a refractive index close to unity, i.e., $|m-1| \ll 1$, has negligible reflectivity and, thus, lets light pass into the sphere unattenuated and unrefracted. If also $x|m-1| \ll 1$, then the light will exit the sphere again essentially unattenuated. However, since the phase velocity of light is slightly less inside the particle, light traveling through the sphere will display a small phase lag as opposed to the incident light. This phenomenon is known as *Rayleigh–Gans scattering*.

As described by van de Hulst [3], taking the appropriate limits reduces equations (12.15) and (12.16) to

$$S_2(\Theta) = S_1(\Theta)\cos\Theta = ix^3(m-1)G(u)\cos\Theta, \tag{12.54}$$

where

$$G(u) = \frac{2}{u^3}(\sin u - u\cos u), \qquad u = 2x\sin\tfrac{1}{2}\Theta. \tag{12.55}$$

The absorption efficiency is identical to the one for Rayleigh scattering, that is,

$$Q_{\text{abs}} = -4\Im\left\{\frac{m^2-1}{m^2+2}\right\}x, \tag{12.56}$$

while the scattering efficiency turns out to be

$$Q_{\text{sca}} = |m-1|^2x^4\int_0^\pi G^2(u)(1+\cos^2\Theta)\sin\Theta\, d\Theta. \tag{12.57}$$

Finally, the phase function for Rayleigh–Gans scattering is now easily determined as

$$\Phi(\Theta) = \frac{2G^2(u)(1+\cos^2\Theta)}{\displaystyle\int_0^\pi G^2(u)(1+\cos^2\Theta)\sin\Theta\, d\Theta}. \tag{12.58}$$

An example of this phase function is included in Fig. 12-5*b* for $x = 5$ and $m = 1.0001$. The phase function displays a strong forward-scattering peak (which increases with increasing size parameter), with very rapid oscillations of varying amplitude into the other directions.

12.6 ANOMALOUS DIFFRACTION

Simple relations for near-dielectric spheres, $|m-1| \ll 1$, can also be obtained for arbitrary values of $x|m-1|$, provided the particles are large, $x \gg 1$. This allows separation of (approximately straight) transmission and diffraction, and is called anomalous diffraction by van de Hulst [3]. For this limiting case the efficiency factors are found from

$$\begin{aligned} Q_{\text{ext}} &= 4\Re\left\{K\big(2x(m-1)i\big)\right\} \\ &= 2 - \frac{4}{p}\cos q\left[e^{-p\tan q}\left(\sin(p-q) + \frac{\cos q}{p}\cos(p-2q)\right) - \frac{\cos q}{p}\cos 2q\right], \end{aligned} \tag{12.59}$$

$$Q_{\text{abs}} = 2K(2p\tan q), \tag{12.60}$$

where

$$K(w) = \frac{1}{2} - \frac{1}{w^2}\left[1-(1+w)\,e^{-w}\right], \tag{12.61}$$

$$p = 2x(n-1), \quad q = \tan^{-1}\frac{k}{n-1}; \quad p\tan q = 2xk. \tag{12.62}$$

Physically, p represents the phase lag experienced by a ray that passes through the center of the sphere. Similar to Rayleigh–Gans scattering, many nonmetallic particles present during combustion come reasonably close to satisfying the $|m-1| \ll 1$ conditions.

12.7 RADIATIVE PROPERTIES OF LARGE SPHERES

If the spheres are very large ($x \gg 1$), very many terms are required in the evaluation of equations (12.15) and (12.16). However, in this case it is sufficient to resort to geometric optics, and one may separate diffraction from reflection and refraction. For very large spheres it is always true that

$$Q_{\text{ext}} = 2. \tag{12.63}$$

This relationship is sometimes called the *extinction paradox* since it states that a large particle removes exactly *twice* the amount of light from the beam as it can intercept, and has been discussed by van de Hulst [3]. Since, for geometric optics, the projected area of a particle for reflection and absorption is πa^2, this means that half of the extinction efficiency is due to diffraction. How much of the rest is due to absorption, and how much due to reflection, depends on the value of the complex index of refraction m, or the reflectivity of the sphere's surface.

In the following we shall determine the scattering properties of *large opaque spheres*, i.e., such spheres for which any ray refracted into the particle will be totally absorbed within, without exiting the sphere at another location. This requires the additional assumption that $kx \gg 1$ (say, 2 or 3). Thus, k may be fairly small as long as $x \gg 1$. A consequence of this is that, for a metal, "large particle" may mean $x > 10$, while for a near-dielectric it may mean $x > 10{,}000$.

While electromagnetic wave theory always assumes optically smooth surfaces, resulting in specular reflection, very large spheres (as compared with wavelength) may have roughness levels at the sphere's surface that are also large as compared with wavelength, resulting in nonspecular reflection. Treatment of very irregular directional behavior for the reflectance is, of course, extremely difficult (as it was for surface transport, cf. Chapter 7). However, the extreme case of perfectly diffuse reflection lends itself to straightforward analysis (similar to the treatment of surface transport in Chapter 5), and is, therefore, also included in the present section.

Diffraction from Large Spheres

The diffraction pattern of light passing through the vicinity of a large sphere is, by Babinet's principle, equal to that of a circular hole with the same diameter [3]. As a consequence the directional behavior of the diffracted light consists of alternating bright and dark rings. The amplitude functions for diffraction have been given by van de Hulst [3] as

$$S_1(\Theta) = S_2(\Theta) = x\frac{J_1(x\sin\Theta)}{\sin\Theta}, \tag{12.64}$$

where J_1 is a Bessel function [19]. Therefore, the phase function for diffraction over a large sphere follows from equation (12.13) (noting that $Q_{\text{sca}} = 1$ for diffraction) as

$$\Phi(\Theta) = 2\frac{i_1 + i_2}{x^2} = 4\frac{J_1^2(x\sin\Theta)}{\sin^2\Theta}. \tag{12.65}$$

This phase function, depicted in Fig. 12-11, demonstrates that almost all energy is scattered forward within a narrow cone of $\Theta < (150/x)^\circ$ from the direction of transmission. Thus, in heat

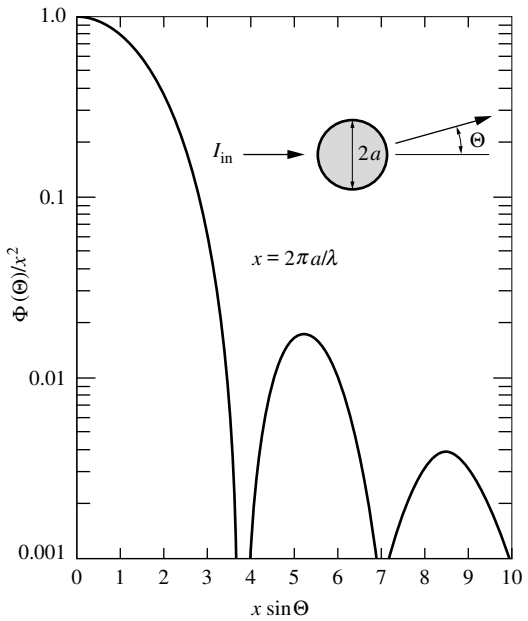

FIGURE 12-11
Phase function for diffraction over a large sphere.

transfer applications we may usually neglect diffraction and treat it as transmission. Then, for large particles without diffraction,

$$Q_{ext} = 1. \tag{12.66}$$

Large Specularly Reflecting Spheres

Consider a specularly reflecting opaque sphere irradiated by an intensity I_i distributed over a thin pencil of rays of solid angle $d\Omega_i$ as shown in Fig. 12-12. Under these conditions the infinitesimal band at an angle β from the incident direction (indicated by shading in the figure) receives radiation from a direction which is off-normal (from its surface) by an angle β. Recalling the definition of intensity as "heat rate per unit area normal to the rays, per unit solid angle, and per unit wavelength," the energy intercepted by the band over a wavelength range of $d\lambda$ is

$$d^2Q_i = I_i\, d\Omega_i\, d\lambda\, (dA_{band} \cos\beta) = I_i\, d\Omega_i\, d\lambda\, 2\pi a \sin\beta\, a\, d\beta\, \cos\beta. \tag{12.67}$$

Of that, the fraction $\rho^s(\beta)$ is reflected into the direction 2β as measured from the incoming pencil of rays. The total heat rate intercepted by the sphere is

$$dQ_i = \int_0^{\pi/2} I_i\, d\Omega_i\, d\lambda\, 2\pi a^2 \sin\beta \cos\beta\, d\beta = I_i\, d\Omega_i\, d\lambda\, \pi a^2, \tag{12.68}$$

while the total reflected (or scattered) heat rate is

$$\begin{aligned} dQ_s &= \int_0^{\pi/2} \rho^s(\beta) I_i\, d\Omega_i\, d\lambda\, 2\pi a^2 \sin\beta \cos\beta\, d\beta \\ &= I_i\, d\Omega_i\, d\lambda\, \pi a^2 2 \int_0^{\pi/2} \rho^s(\beta) \sin\beta \cos\beta\, d\beta = \rho^s I_i\, d\Omega_i\, d\lambda\, \pi a^2, \end{aligned} \tag{12.69}$$

where ρ^s is the hemispherical reflectance, averaged over all incoming directions [cf. equation (3.46)]:

$$\rho^s = 2 \int_0^{\pi/2} \rho^s(\beta) \sin\beta \cos\beta\, d\beta. \tag{12.70}$$

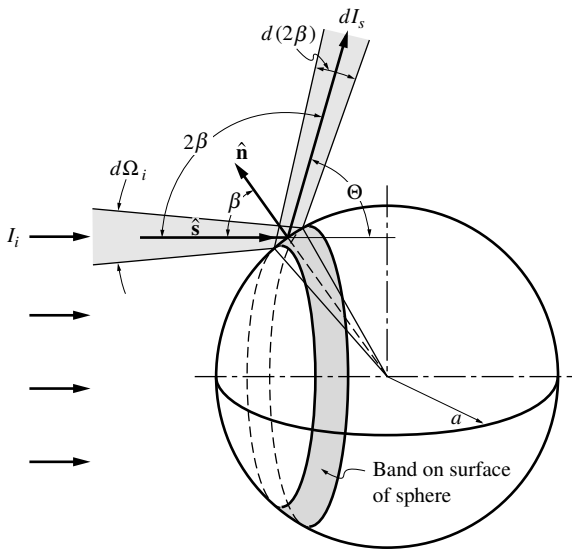

FIGURE 12-12
Scattering of incident radiation by a large specularly reflecting sphere.

Thus, the scattering efficiency for a large, opaque, specularly reflecting particle is simply

$$Q_{\text{sca}} = \frac{dQ_s}{dQ_i} = \rho^s, \tag{12.71}$$

and the absorption efficiency follows as

$$Q_{\text{abs}} = Q_{\text{ext}} - Q_{\text{sca}} = 1 - \rho^s = \alpha, \tag{12.72}$$

that is, the hemispherical absorptivity.

To evaluate the scattering phase function we consider the amount of energy scattered into any given direction Θ, where Θ is measured from the transmission direction $\hat{\mathbf{s}}$, as also indicated in Fig. 12-12. It is clear that, for a homogeneous sphere, the scattered intensity can only vary with the polar angle Θ (and not azimuthally). Furthermore, for a specularly reflecting sphere the outgoing intensity in a certain direction Θ can only come from a single position on the sphere's surface. For example, radiation scattered into the direction $\Theta = \pi - 2\beta$ comes from the shaded band in Fig. 12-12. Recalling that the scattering phase function is defined as $4\pi \times$ scattered intensity/total scattered heat flux [cf. equation (10.15)] we get, for $\Theta = \pi - 2\beta$ or $\beta = (\pi - \Theta)/2$,

$$\begin{aligned}\Phi(\Theta) &= 4\pi \frac{\rho^s(\beta)\, d^2Q_i/d\Omega_r}{dQ_s} \\ &= 4\pi\rho^s\left(\frac{\pi-\Theta}{2}\right) \frac{I_i\, d\Omega_i\, d\lambda\, 2\pi a^2 \sin\beta\cos\beta\, d\beta/d\Omega_r}{\rho^s I_i\, d\Omega_i\, d\lambda\, \pi a^2}.\end{aligned} \tag{12.73}$$

The solid angle for the reflection is best visualized by letting the reflected intensity fall upon a concentric (and very large) sphere of radius R. The solid angle is then the area of the illuminated band divided by R^2, or

$$d\Omega_r = 2\pi \sin 2\beta\, d(2\beta), \tag{12.74}$$

leading to

$$\Phi(\Theta) = \rho^s\left(\frac{\pi-\Theta}{2}\right)\Big/\rho^s. \tag{12.75}$$

Alternatively, we could use the fact that the scattering phase function is proportional to intensity into any given direction, and then normalize the resulting expression with equation (10.17). The

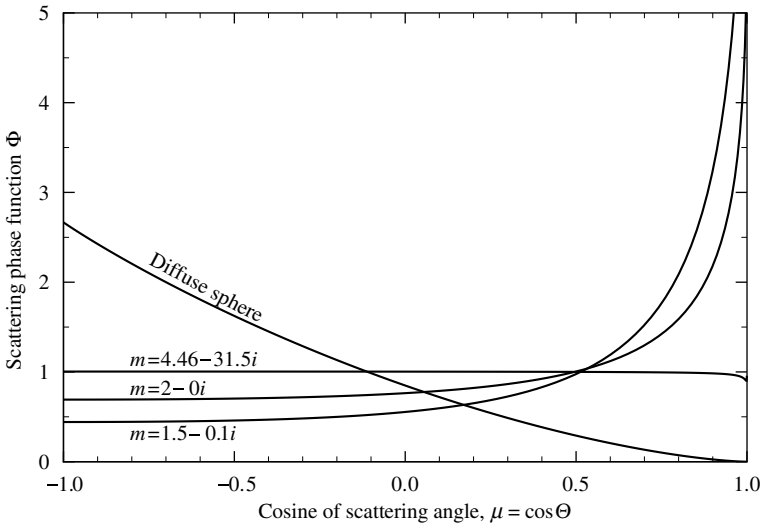

FIGURE 12-13
Scattering phase functions for large spheres of various materials.

actual directional scattering behavior (or the behavior of the phase function) depends on the material of which the particles are made. Figure 12-13 shows a comparison of the phase function between a "typical" metal (aluminum at 3.1 μm with an index of refraction of $m = 4.46{-}31.5i$) and a "typical" dielectric ($m = 2$).[1] These two phase functions should be compared with Fig. 12-5*c,d*, which are for identical materials but for a smaller size parameter (and are shown in a polar rather than a Cartesian plot). Since the size parameter in Fig. 12-5*c,d* is fairly large ($x = 10$), the major difference between Fig. 12-5*c,d* and Fig. 12-13 lies in the omission of diffraction in Fig. 12-13. For large particles all materials have their maximum scattering into the forward direction, $\Theta = 0$, since $\rho^s(\pi/2) = 1$ always. However, this peak is considerably more pronounced for dielectrics, and is hardly noticeable for the metal because of the dip in reflectance at near-grazing angles (compare also Fig. 2-11, which shows the directional variation of the reflectance of aluminum). Because of their relatively high reflectance at all directions, large metallic particles tend to be almost isotropic scatterers.

Example 12.2. Consider glass particles with a complex index of refraction $m = 1.5 - 0.1i$ and a density of $\rho_{\text{glass}} = 2\,\text{g/cm}^3$, suspended in an inert gas, with a particle loading ratio of 1 kg of particles per m^3 of suspension volume. Particle sizes range between 100 μm and 1000 μm, with an equal distribution over all sizes by weight-%. Determine the absorption coefficient, the scattering coefficient, and the phase function for the infrared ($3\,\mu\text{m} < \lambda < 10\,\mu\text{m}$).

Solution
First, we need to determine the particle distribution function by number (rather than mass). Since the mass distribution function is a constant we get

$$m(a) = \frac{1\,\text{kg/m}^3}{(1000-100)\,\mu\text{m}} = \tfrac{4}{3}\pi a^3 \rho_{\text{glass}} n(a), \quad 100\,\mu\text{m} \le a \le 1000\,\mu\text{m},$$

$$n(a) = \frac{3m(a)}{4\pi a^3 \rho_{\text{glass}}} = 1.3226 \times 10^{-7}\,\mu\text{m}^{-1}/a^3, \quad 100\,\mu\text{m} \le a \le 1000\,\mu\text{m}.$$

Next we need to determine the range of the size parameter x to see whether Rayleigh scattering, Lorenz–Mie scattering, or large-particle scattering must be considered. The minimum value for x will occur for the smallest particle at the longest wavelength, or

$$x_{\min} = \frac{2\pi a_{\min}}{\lambda_{\max}} = \frac{2\pi 100}{10} = 62.83 \gg 1,$$

[1]Note that in the case of a dielectric the absorptive index k is assumed negligible as compared with the refractive index n, but k is assumed large enough to make the spheres opaque.

$$(kx)_{\min} = 6.283 \gg 1,$$

that is, the large-particle assumption will be acceptable for all conditions encountered in this example. Thus, the absorption and scattering coefficients may be related to the hemispherical emissivity of the glass. Since for this glass $k \ll n$, the material behaves essentially like a dielectric, and the hemispherical emissivity may be found from Fig. 3-19 or equation (3.82). Either method leads to $\epsilon = \alpha = 1 - \rho = 0.91$. The absorption and scattering coefficients may then be calculated from equations (12.39) and (12.38) as

$$\begin{aligned}
\kappa_\lambda &= \pi \int_0^\infty \alpha a^2 n(a)\, da = \pi\alpha \int_{100\,\mu\text{m}}^{1000\,\mu\text{m}} a^2\, \frac{1.3226 \times 10^{-7}}{\mu\text{m}\, a^3}\, da \\
&= 1.3226 \times 10^{-7}\, \mu\text{m}^{-1} \pi\alpha \ln \frac{1000}{100} = 9.60 \times 10^{-3} \alpha\, \text{cm}^{-1} \\
&= 8.74 \times 10^{-3}\, \text{cm}^{-1}, \\
\sigma_{s\lambda} &= 9.60 \times 10^{-3} \rho\, \text{cm}^{-1} = 0.86 \times 10^{-3}\, \text{cm}^{-1}.
\end{aligned}$$

The scattering phase function must be evaluated from equation (12.75) and is also included in Fig. 12-13. Because of the small value for k, the directional behavior is very similar to that of the perfect dielectric ($m = 2$), but the forward-scattering peak is more pronounced because of the smaller refractive index.

Large Diffusely Reflecting Spheres

In equations (12.67) through (12.72) the directional characteristics of the sphere reflectance did not enter the development. Thus, for a diffusely reflecting sphere the amount of incident radiation on a surface element, as well as the expression for the heat flux reflected into all directions, is the same as for a specularly reflecting sphere. Therefore, equations (12.67) through (12.72) also hold for the diffusely reflecting sphere, or

$$Q_{\text{abs}} = \alpha, \tag{12.76}$$

$$Q_{\text{sca}} = \rho. \tag{12.77}$$

However, while for a specularly reflecting sphere the energy scattered into any given direction resulted from reflection from a single location on the sphere's surface, this is not true for a diffusely reflecting sphere. This complicates the development for the scattering phase function a bit. Consider Fig. 12-14: Incident radiation traveling into the direction of the unit vector $\hat{\mathbf{s}}_i$ illuminates one half of the diffusely reflecting sphere. An observer, located far away from the sphere in the direction of $\hat{\mathbf{s}}_o$, sees a different half of the sphere, part of which is illuminated by the incident radiation (shown by shadowing), part of which is in the shade. This illuminated region seen by the observer has the shape of a circular wedge similar to a slice of lemon. To describe the surface in polar coordinates it is most convenient to define the plane formed by the two unit vectors $\hat{\mathbf{s}}_i$ and $\hat{\mathbf{s}}_o$ to be the x-y-plane with polar angle β measured from the z-axis and the azimuthal angle ψ measured from the negative x-axis as indicated in Fig. 12-14. With this coordinate system the normal to a surface element in the illuminated region may be expressed as

$$\hat{\mathbf{n}}(\beta, \psi) = -\sin\beta \cos\psi\, \hat{\mathbf{i}} + \sin\beta \sin\psi\, \hat{\mathbf{j}} + \cos\beta\, \hat{\mathbf{k}}, \tag{12.78}$$

and also

$$\hat{\mathbf{s}}_i = \hat{\mathbf{i}}, \qquad \hat{\mathbf{s}}_o = \cos\Theta\, \hat{\mathbf{i}} + \sin\Theta\, \hat{\mathbf{j}}. \tag{12.79}$$

The energy reflected from an infinitesimal surface area is, as developed in equation (12.67),

$$d^2 Q_s = \rho I_i\, d\Omega_i\, d\lambda\, [dA(-\hat{\mathbf{n}} \cdot \hat{\mathbf{s}}_i)], \tag{12.80}$$

where dA is two-dimensionally infinitesimal as indicated in Fig. 12-14 (i.e., not a ring as in the previous section, Fig. 12-12). Thus, the *radiosity* at that location, because of diffuse reflection of incident radiation, is

$$dJ = \rho I_i\, d\Omega_i\, d\lambda\, (-\hat{\mathbf{n}} \cdot \hat{\mathbf{s}}_i). \tag{12.81}$$

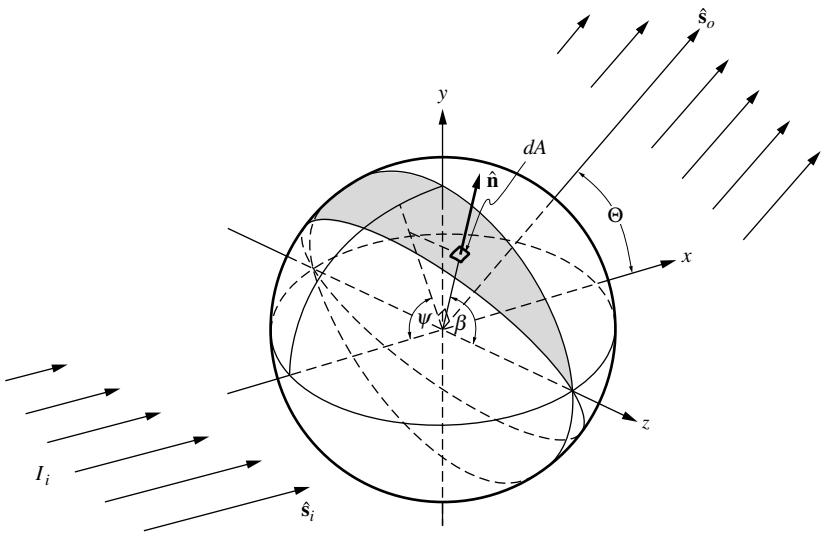

FIGURE 12-14
Scattering of incident radiation by a large diffusely reflecting sphere.

Some of the reflected radiation will travel toward the observer into the direction of $\hat{\mathbf{s}}_o$. If we assume the observer stands on a large sphere with radius $R \gg a$, then the heat flux through a surface element dA_R on the large sphere due to reflection from the small sphere is

$$dI_s\, d\Omega = \int_{A_{\text{shaded}}} dJ\, dF_{dA-dA_R}\, dA, \tag{12.82}$$

where

$$dF_{dA-dA_R} = \frac{\hat{\mathbf{n}} \cdot \hat{\mathbf{s}}_o\, dA_R}{\pi R^2} = \frac{1}{\pi} \hat{\mathbf{n}} \cdot \hat{\mathbf{s}}_o\, d\Omega \tag{12.83}$$

is the view factor between dA and dA_R, $\hat{\mathbf{n}} \cdot \hat{\mathbf{s}}_o$ is the cosine of the angle between the surface normal at dA and the line to dA_R, while the surface normal at dA_R points directly to the particle. Thus,

$$dI_s = \frac{1}{\pi} \int_{A_{\text{shaded}}} dJ\, \hat{\mathbf{n}} \cdot \hat{\mathbf{s}}_o\, dA, \tag{12.84}$$

and, again recalling that the scattering phase function is equal to $4\pi \times$ scattered intensity/total scattered heat flux, we get

$$\begin{aligned}
\Phi(\hat{\mathbf{s}}_i, \hat{\mathbf{s}}_o) &= 4\pi\, dI_s / dQ_s = 4 \int_{A_{\text{shaded}}} (\rho I_i\, d\Omega_i\, d\lambda)(-\hat{\mathbf{n}} \cdot \hat{\mathbf{s}}_i)(\hat{\mathbf{n}} \cdot \hat{\mathbf{s}}_o)\, dA \Big/ \rho I_i\, d\Omega_i\, d\lambda\, \pi a^2 \\
&= \frac{4}{\pi a^2} \int_{A_{\text{shaded}}} (-\hat{\mathbf{n}} \cdot \hat{\mathbf{s}}_i)(\hat{\mathbf{n}} \cdot \hat{\mathbf{s}}_o)\, dA \\
&= \frac{4}{\pi a^2} \int_{\frac{\pi}{2}-\Theta}^{\frac{\pi}{2}} \int_0^{\pi} \sin\beta \cos\psi \sin\beta (\sin\psi \sin\Theta - \cos\psi \cos\Theta)\, a^2 \sin\beta\, d\beta\, d\psi,
\end{aligned}$$

which may readily be integrated to yield

$$\Phi(\Theta) = \frac{8}{3\pi}(\sin\Theta - \Theta \cos\Theta). \tag{12.85}$$

The phase function for diffuse spheres, equation (12.85), is also depicted in Fig. 12-13. Unlike for specularly reflecting spheres, the phase function for diffusely reflecting spheres displays a strong backward-scattering peak, and it is independent of the reflectance (or the complex index of refraction) of the materials.

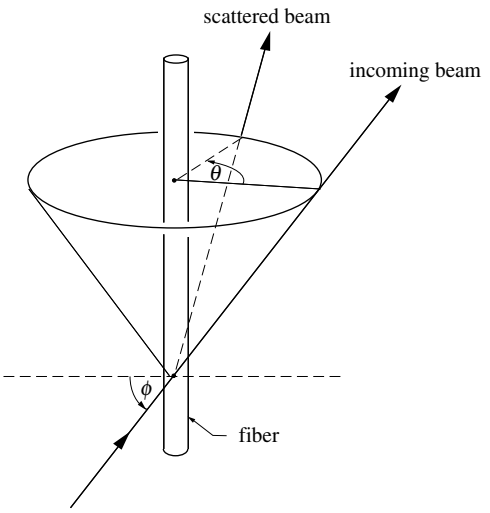

FIGURE 12-15
Scattering of incident radiation by a long cylinder.

Particle Beds

The scattering regime map of Fig. 12-2 suggests that independent scattering may be assumed for packed and fluidized beds with particle volume fractions as large as 0.7 [5]. However, the classical continuum theory for radiative transfer in particulate media is based on the assumption of infinitesimally small particle size and, thus, negligible shading. Particle beds generally contain relatively large particles ($x \gg 1$) and, combined with large volume fractions, shading can no longer be ignored [27]. Brewster [28] proposed a simple correction to equation (12.29) as

$$\beta_\lambda = \frac{\pi a^2 N_T Q_{\text{ext}}}{1 - f_v} = \frac{3 f_v}{(1 - f_v)a}, \tag{12.86}$$

where uniform particle size has been assumed, and $Q_{\text{ext}} = 1$ for large particles. Comparison with stochastic Monte Carlo simulations [27] showed near-perfect agreement. Another, more recent ray tracing algorithm for densely packed spheres also attests to the accuracy of equation (12.86) [29].

12.8 ABSORPTION AND SCATTERING BY LONG CYLINDERS

Scattering from cylinders has been studied for almost as long as that from spheres, starting with Lord Rayleigh looking at infinitely long cylinders at normal incidence. In the area of radiative heat transfer scattering from cylinders has become of interest only very recently, to predict transfer rates through optical fibers and fibrous insulation.

Consider a cylinder of length L and radius a, with its axis pointed into the direction of $\hat{\mathbf{s}}_f$, that is irradiated obliquely by electromagnetic waves propagating into direction $\hat{\mathbf{s}}$ as indicated in Fig. 12-15. For cylinders it is common to define the angle of incidence with respect to the normal to the cylinder axis, i.e., $\hat{\mathbf{s}} \cdot \hat{\mathbf{s}}_f = \sin\phi$ as shown. Similar to waves impinging obliquely on flat surfaces (see Chapter 2), we need to distinguish between two polarization components: the transverse magnetic (TM, or "Case I"; no magnetic vector component in the $\hat{\mathbf{s}}_f$-direction) mode, and the transverse electric (TE, or "Case II"; no electric vector component in the $\hat{\mathbf{s}}_f$-direction) mode. For short cylinders the scattering behavior is very similar to that of spheres, but with increasing L/a-ratio scattering becomes more and more confined to a conical surface (rather than being spread out over all 4π solid angles).

For infinitely long cylinders ($L/a \to \infty$) all scattering is confined to the conical surface described by $\hat{\mathbf{s}}_f$ and $\hat{\mathbf{s}}$ as indicated in Fig. 12-15. The nondimensional polarized scattering intensities can be calculated for this case as [16]

$$i_{11}(m,x,\phi,\theta) = |T_{11}|^2 = \left| b_{0\mathrm{I}} + 2\sum_{n=1}^{\infty} b_{n\mathrm{I}} \cos n\theta \right|^2, \tag{12.87a}$$

$$i_{12}(m,x,\phi,\theta) = |T_{12}|^2 = \left| 2\sum_{n=1}^{\infty} a_{n\mathrm{I}} \sin n\theta \right|^2, \tag{12.87b}$$

$$i_{21}(m,x,\phi,\theta) = |T_{21}|^2 = \left| 2\sum_{n=1}^{\infty} b_{n\mathrm{II}} \sin n\theta \right|^2, \tag{12.87c}$$

$$i_{22}(m,x,\phi,\theta) = |T_{22}|^2 = \left| a_{0\mathrm{II}} + 2\sum_{n=1}^{\infty} a_{n\mathrm{II}} \cos n\theta \right|^2. \tag{12.87d}$$

As for spheres the a_n and b_n can be expressed in terms of Bessel and Hankel functions, and are given by Kerker [16]. For unpolarized incident radiation the nondimensional intensity is evaluated as

$$i(m,x,\phi,\theta) = \frac{1}{2}(i_{11} + i_{12} + i_{21} + i_{22}); \qquad i_{12} = i_{21}, \tag{12.88}$$

and extinction and scattering cross-sections and efficiencies are evaluated from

$$Q_{\mathrm{ext}} = \frac{C_{\mathrm{ext}}}{2a} = \frac{2}{x}\Re\Big(T(\theta=0)\Big) = \frac{1}{x}\Re\left\{ b_{0\mathrm{I}} + a_{0\mathrm{II}} + 2\sum_{n=1}^{\infty}(b_{n\mathrm{I}} + a_{n\mathrm{II}}) \right\} \tag{12.89}$$

$$\begin{aligned} Q_{\mathrm{sca}} &= \frac{C_{\mathrm{sca}}}{2a} = \frac{1}{\pi x}\int_0^{2\pi} i\Big(m,x,\phi,\theta\Big)\, d\theta \\ &= \frac{1}{x}\left\{ |b_{0\mathrm{I}}|^2 + |a_{0\mathrm{II}}|^2 + \sum_{n=1}^{\infty}\Big(|b_{n\mathrm{I}}|^2 + |b_{n\mathrm{II}}|^2 + |a_{n\mathrm{I}}|^2 + |a_{n\mathrm{II}}|^2\Big)\right\}, \end{aligned} \tag{12.90}$$

where, as for spheres, $x = 2\pi a/\lambda$, but cross-sections are per unit length of cylinder (i.e., have units of length). The phase function for a single, infinite cylinder is given by [30]

$$\Phi(\Theta,\phi) = \frac{i(\theta,\phi)\delta(\phi-\phi')}{\int_0^{2\pi} i(\theta,\phi)\, d\theta}, \quad \cos\theta = (\cos\Theta - \sin^2\phi')/\cos^2\phi', \tag{12.91}$$

where $\delta(\phi-\phi')$ is the Dirac-delta function,[2] and Θ is again the scattering angle away from the $\hat{\mathbf{s}}$-direction, which is related to polar angle ϕ' and azimuthal angle θ as given.

The behavior of infinitely long fibers has been investigated by several researchers, notably the group around Tong [31–36] and by Lee [30, 37–43] and others [44–47]. Some of these investigations have concentrated on scattering by single fibers [34, 35, 37], others on effects of dependent scattering [40–42, 44], but most deal with the effects of various fiber arrangements. For a random arrangement of infinitely long fibers with size distribution $n(a)$, extinction and scattering properties can be determined from [37]:

$$\beta_\lambda(m) = \int_0^{\infty}\int_0^{\pi/2} C_{\mathrm{ext}}(m,x,\phi)\cos\phi\, d\phi\, n(a)\, da, \tag{12.92}$$

[2] First defined in Section 11.9, equation (11.99).

$$\sigma_{s\lambda}(m) = \int_0^\infty \int_0^{\pi/2} C_{\text{sca}}(m, x, \phi) \cos\phi \, d\phi \, n(a) \, da, \tag{12.93}$$

$$\Phi_\lambda(m, \Theta) = \frac{1}{\sigma_{s\lambda}} \frac{4\lambda}{\pi^2} \int_0^\infty \int_0^{\pi/2} \frac{i(\theta)}{\sin\theta \cos\phi} \, d\phi \, n(a) \, da,$$

$$\cos\theta = \left(\cos\Theta - \sin^2\phi\right) \Big/ \cos^2\phi. \tag{12.94}$$

12.9 APPROXIMATE SCATTERING PHASE FUNCTIONS

It is clear from Figs. 12-3 and 12-8 that radiative properties of particles may display strong oscillatory behavior with size parameter and, therefore, wavelength, particularly for the case of large, monodisperse, dielectric particles. Even more bothersome is the fact that the scattering phase function may undergo strong angular oscillations at any given single wavelength, again particularly for the case of large, monodisperse, dielectric particles (cf. Figs. 12-5, 12-6, 12-7). Since radiative calculations for media with spectrally varying properties are generally carried out on a spectral basis with subsequent integration over all relevant wavelengths, this fact means that these spectral oscillations are somewhat inconvenient, but they do not make the analysis intractable. Strong angular oscillations in the scattering phase function, on the other hand, will enormously complicate the analysis for any given wavelength. Indeed, most solution methods described in the following chapters cannot accept highly oscillatory phase functions, or else they must be carried to unacceptably high orders or node numbers. It is, therefore, common practice to approximate oscillatory phase functions by simpler expressions with more regular behavior.

It is observed that large particles generally have strong forward-scattering peaks (due to diffraction, cf. Figs. 12-6 and 12-7). Indeed, if $x \to \infty$, half of the total extinction is due to diffraction into near-forward directions, as described in Section 12.7. Since diffraction was neglected (i.e., treated as transmission) in that section, the phase functions for large particles are in fact simplified. If either geometric optics cannot be used or diffraction effects must be retained for other reasons, then the approximate phase function must accommodate the strong forward-scattering peak. To this purpose many investigators have used the *Henyey–Greenstein phase function*,

$$\Phi_{HG}(\Theta) = \frac{1 - g^2}{[1 + g^2 - 2g\cos\Theta]^{3/2}}, \tag{12.95}$$

where g is the asymmetry factor. Sometimes the Henyey–Greenstein function is written in the form of a Legendre polynomial series, or

$$\Phi_{HG}(\Theta) = 1 + \sum_{n=1}^{\infty} (2n + 1) g^n P_n(\cos\Theta). \tag{12.96}$$

Thus, this expression is equivalent to equation (12.24) with approximate values for the A_n being related to the asymmetry factor. A representative comparison between Lorenz–Mie and Henyey–Greenstein phase functions is given in Fig. 12-16 for a dielectric with index of refraction $m = n = 1.33$ and size parameter $x = 300$ (water droplets). Both van de Hulst [48] and Hansen [49] have shown that the Henyey–Greenstein formulation gives very accurate results for radiative heat fluxes as long as the particles are nondielectric: Dielectric particles may have a relatively strong backward-scattering peak besides a strong forward-scattering peak. This situation cannot be described by the asymmetry factor alone, and the Henyey–Greenstein formulation must fail. That neglect of backward-scattering peaks can cause considerable error in heat flux calculations has been shown by Modest and Azad [25].

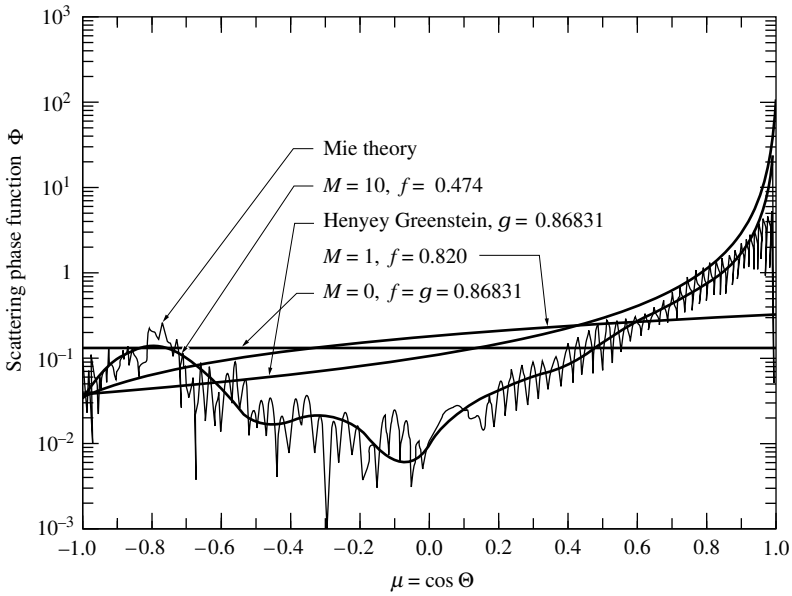

FIGURE 12-16
Comparison of Lorenz–Mie, Henyey–Greenstein, linear-anisotropic, and isotropic phase functions for water droplets ($m = 1.33,\ x = 100$).

For many calculations the Henyey–Greenstein phase function is still too complicated. As mentioned earlier, in heat transfer applications forward scattering may usually be treated as transmission. This fact has led a number of researchers to the use of so-called *Dirac-delta* or *Delta–Eddington approximations*, where the forward-scattering peak is separated from the rest of the scattering phase function by

$$\Phi(\Theta) \approx 2f\,\delta(1-\cos\Theta) + (1-f)\,\Phi^*(\Theta), \tag{12.97}$$

where Φ^* is the new approximate phase function, f is a forward scattering fraction to be determined, and δ is the *Dirac-delta function*. Substitution of equation (12.97) into equation (10.17) shows that the approximate phase function is properly normalized, that is,

$$\frac{1}{4\pi}\int_{4\pi}\Phi^*(\Theta)\,d\Omega = 1. \tag{12.98}$$

Different authors have used different approaches to define f and Φ^*. Potter [50] was one of the first to use the following scheme for his work on atmospheric scattering. He truncated the peak by extrapolating the phase function from directions outside the peak into the forward direction; otherwise he left the phase function unchanged. Not surprisingly, his method produced excellent results, but it still leaves the approximate phase function in a rather complex form.

It appears more promising to express the approximate phase function as a truncated Legendre series,

$$\Phi^*(\Theta) = 1 + \sum_{n=1}^{M} A_n^* P_n(\cos\Theta), \tag{12.99}$$

where the constant M is the chosen order of approximation, mostly taken as $M = 1$ (linear-anisotropic scattering) [25, 51–53], or $M = 0$ (isotropic scattering) [52], while higher-order approximations have been carried out by Crosbie and Davidson [52]. There is considerable disagreement among authors about the criteria to be used to determine the forward fraction f as well as the coefficients A_n^*. Both Joseph and coworkers [51] and Crosbie and Davidson [52]

agreed that at least one of the *moments* of equation (12.97) should be satisfied: Multiplying equation (12.97) by $P_m(\Theta)$ and integrating over all Θ results in

$$\int_0^\pi \Phi(\Theta)P_m(\cos\Theta)\,d\Theta = \int_0^\pi 2f\delta(1-\cos\Theta)P_m(\cos\Theta)\,d\Theta + (1-f)\sum_{n=1}^{M}\int_0^\pi A_n^* P_n(\cos\Theta)\,P_m(\cos\Theta)\,d\Theta, \quad (12.100)$$

or, using the fact that Legendre polynomials are orthogonal functions over the interval $(0, \pi)$ [19],

$$(1-f)A_m^* = A_m - (2m+1)f, \quad m = 1, 2, \ldots. \quad (12.101)$$

If the approximate phase function is to be *isotropic*, equation (12.101) yields, with $A_1^* = 0$,

$$f = \frac{A_1}{3} = g, \quad (12.102)$$

and

$$\Phi(\Theta) \approx 2g\delta(1-\cos\Theta) + (1-g). \quad (12.103)$$

Joseph and colleagues [51] developed an approximate *linear-anisotropic* phase function. They employed equation (12.101) for the first two moments to find f and A_1^*, using an approximate value of $A_2 \approx 5g^2$ (from the Henyey–Greenstein phase function). However, their approximate phase function may turn out to be negative for some back scattering directions, which is physically impossible. Crosbie and Davidson [52] overcame this difficulty by applying the second moment only conditionally. From the first moment it follows that

$$A_1^* = 3\frac{g-f}{1-f}. \quad (12.104)$$

Requiring the phase function to be positive for all angles is equivalent to $|A_1^*| \le 1$, or

$$\frac{1}{2}(3g-1) \le f \le g. \quad (12.105)$$

Instead of using the second moment directly, i.e., $f = A_2/5$, they require $|f - A_2/5|$ to be a minimum without violating equation (12.105). This method can readily be extended to arbitrarily high orders. Their linear-anisotropic and order-10 phase function approximations are also included in Fig. 12-16 for water droplets. It should be noted that this method will work only for *positive* asymmetry factors. In the case of $g < 0$ the method breaks down and $f = 0$ should be used. Even then one may find $A_1^* < -1$, in which case one has to force $A_1^* = -1$ to avoid negative forward scattering. The method will break down completely for strong backward-scattering peaks.

None of the above approximations allows for simultaneous forward- and backward-scattering peaks. Modest and Azad [25] have shown that neglecting the backward-scattering peaks that may appear in dielectrics may cause considerable error in heat flux calculations. Thus, they proposed a *double Dirac-delta phase function* approximation. However, this model severely complicates the RTE by requiring a $I(-\hat{\mathbf{s}})$ term (backward intensity).

Example 12.3. Calculate approximate phase functions for monodisperse suspensions of large specular dielectric spheres ($m = 2$) and diffusely reflecting spheres, using the Henyey–Greenstein function, and the Crosbie and Davidson model.

Solution

The Henyey–Greenstein function requires the calculation of the asymmetry factor

$$g = \frac{A_1}{3} = \frac{1}{2}\int_{-1}^{+1} \Phi(\mu)\mu\,d\mu,$$

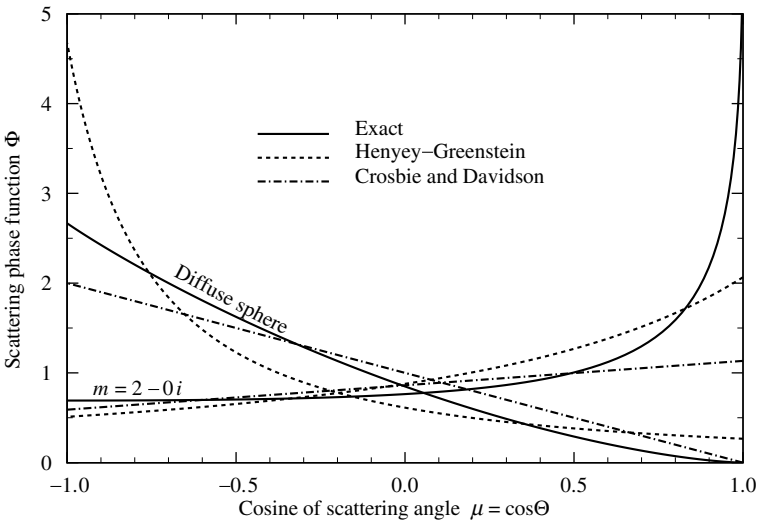

FIGURE 12-17
Scattering phase function approximations for Example 12.3.

where μ is the cosine of the scattering angle. The Crosbie and Davidson approximation requires the calculation of g as well as the calculation of

$$\frac{A_2}{5} = \frac{1}{2}\int_{-1}^{+1} \Phi(\mu) P_2(\mu)\, d\mu.$$

Numerical integration of the phase function yields for the specular dielectric spheres $g = 0.229$ and $A_2/5 = 0.138$. Since $A_2/5 < g$ it follows for the Crosbie and Davidson model that $f = A_2/5 = 0.138$ and, from equation (12.104), $A_1^* = 0.315$. Both approximate phase functions are shown in Fig. 12-17 together with the exact expression. The Henyey–Greenstein function does not try to remove the forward-scattering peak, but is unable to follow the sharp peak for large μ. The Crosbie–Davidson model follows the actual function well, except for the forward peak that has been removed.

The integration for the diffuse-sphere phase function could be carried out analytically but is rather tedious. Numerical integration of the phase function yields for the diffuse spheres $g = -0.444$ and $A_2/5 = 0.062$. Since $g < 0$, the scattering is predominantly backward and the Crosbie and Davidson model cannot be applied. Thus, for this model, we force $f = 0$ and, from equation (12.104), $A_1^* = -1.333$; since this would result in negative values for forward directions we also force $A_1^* = -1$. It is seen that the Henyey–Greenstein function does not work very well for back scattering, while the Crosbie and Davidson model gives acceptable results.

12.10 RADIATIVE PROPERTIES OF IRREGULAR PARTICLES AND AGGREGATES

In practical applications particles are rarely, if ever, homogeneous spheres or long cylinders. As noted earlier, averaging over millions of irregularly shaped particles tends to give results very close to those found with the uniform sphere assumption [1]. However, if the average shape of irregular particles does not resemble a sphere or a long fiber, more advanced methods must be employed to study their interaction with electromagnetic waves. Over the years numerous exact and approximate methods have appeared in the literature, recently reviewed by Mishchenko [54] and Wriedt [55], the latter also listing freely available computer codes. An extensive description of general disperse systems has been given by Dombrovsky and Baillis [2]. An in-depth discussion of the treatment of irregular particles is beyond the scope of this text, and

the reader is directed toward these three exhaustive references. We will give here only a very brief account of the perhaps most popular methods, the *cluster T-matrix method*, the *generalized multisphere Mie solution*, and the *discrete dipole approximation*.

The Cluster T-Matrix Method

The method goes back to 1965 as proposed by Waterman [56], and a detailed description is provided in Mishchenko and coworkers [57]. While the method can be applied to particles of any shape, it is best suited for rotationally symmetric particles, and can be readily applied to multiparticle clusters, such as fractal aggregates. In the T-matrix method the incident, internal, and scattered electromagnetic fields for the individual particles are expanded into vector spherical harmonics. Coefficients of the scattered field are linearly related to those of the incident field by a matrix called the T- (or transition) matrix. Linearity of Maxwell's equations then allows the determination of the scattered field of an agglomerate through superposition. One of the advantages of the T-matrix method is that, once the matrix has been computed, it can be applied to arbitrary incidence angles, i.e., the method provides not only scattering and extinction coefficients, but also directional scattering information, which can be of great importance in laser scattering diagnostics. The method has been gathering considerable popularity and, in particular, has been applied to multisphere clusters, such as soot aggregates [58–62]. Several T-matrix computer codes are freely available from [63, 64].

The Generalized Multisphere Mie Solution

Like the cluster T-matrix method the generalized multisphere Mie solution (GMM) is also an exact method for scattering from clusters of small particles. In fact, the method shares many features with the T-matrix method, but there are also substantial differences, such as different treatment of far-field interference and in translating field expansions between displaced reference systems [65, 66]. The method was developed by Xu [67, 68], and enjoys increasing popularity for the modeling of scattering from soot aggregates [69–71]. A GMM computer code may be downloaded from [72].

The Discrete Dipole Approximation

Another popular method to deal with scattering from aggregates of small particles is the discrete dipole approximation. In the limit of small point masses (i.e., individual atoms) the particles can be thought of as electrical dipoles, which then allows for an exact formulation of the resulting electromagnetic field. To make the problem manageable, a particle or aggregate may be subdivided into a relatively small number of identical elements, each containing many atoms, but small enough to be represented as a dipole oscillator. The vector amplitude of the field scattered by each dipole is determined iteratively, and the total scattered field is obtained as the sum of all the individual dipole fields. The method was first formulated by Purcell and Pennypecker [73]. It appears to be particularly well suited to model aggregates of many identical primary particles, such as soot, and has been employed, for example, by [74, 75].

12.11 RADIATIVE PROPERTIES OF COMBUSTION PARTICLES

Undoubtedly, some of the most important engineering applications of thermal radiation are in the areas of the combustion of gaseous, liquid (usually in droplet form), or solid (often pulverized) fuels, be it for power production or for propulsion. During combustion thermal radiation will carry energy directly from the combustion products to the burner walls, often at rates higher than for convection. In the case of liquid and solid fuels thermal radiation also plays

TABLE 12.2
Representative values for the complex index of refraction in the near infrared for different coals and ashes [84].

Particle Type	$m = n - ik$
carbon	$2.20 - 1.12i$
anthracite	$2.05 - 0.54i$
bituminous	$1.85 - 0.22i$
lignite	$1.70 - 0.066i$
fly ash	$1.50 - 0.020i$

an important role in the preheating of the fuel and its ignition. Nearly all flames are visible to the human eye and are, therefore, called *luminous* (sending out light). Apparently, there is some radiative emission from within the flame at wavelengths where there are no vibration–rotation bands for any combustion gases. This luminous emission is today known to come from tiny *char* (almost pure carbon) particles, called *soot*, which are generated during the combustion process. The "dirtier" the flame is (i.e., the higher the soot content), the more luminous it is. A review of the importance of radiative heat transfer in combustion systems has been given by Sarofim and Hottel [76].

All combustion processes are very complicated. Usually there are many intermediate chemical reactions in sequence and/or parallel, intermittent generation of a variety of intermediate species, generation of soot, agglomeration of soot particles, and subsequent partial burning of the soot. Since thermal radiation contributes strongly to the heat transfer mechanism of the combustion, any understanding and modeling of the process must include knowledge of the radiation properties of the combustion gases as well as any particulates that are present. The most important particles are the relatively large coal and fly ash particles formed during the combustion of pulverized coal as well as the very small soot particles. Because of their great importance, these suspensions will be treated in some detail below.

Pulverized Coal and Fly Ash Dispersions

To calculate the radiative properties of arbitrary size distributions of coal and ash particles, one must have knowledge of their complex index of refraction as a function of wavelength and temperature. Data for carbon and different types of coal indicate that its real part, n, varies little over the infrared and is relatively insensitive to the type of coal (e.g., anthracite, lignite, bituminous), while the absorptive index, k, may vary strongly over the spectrum and from coal to coal [77–79]. The composition of fly ash and, therefore, its optical properties may vary greatly from coal to coal. The few data in the literature [80–83] report consistent values for the refractive index ($n \approx 1.5$) and widely varying values for the absorptive index. Wall and coworkers [82] calculated the absorptive index for a number of Australian coals (based on their ash composition), and found that k varied between 0.008 and 0.020. Nothing at all appears to be known about the temperature dependence of these optical properties. A summary of representative values for the optical constants of coals and ashes has been reported by Viskanta and colleagues [84] and is reproduced in Table 12.2.

A first attempt to establish formulae for extinction by carbon particles was made by Tien and coworkers [85], who looked at a single index of refraction ($m = 1.5 - 0.5i$) for a gamma size distribution of particles [cf. equation (12.34)]. They found a relatively simple (but not very accurate) smooth correlation for the extinction coefficient β. Buckius and Hwang [86] carried out a large number of Lorenz–Mie calculations for a variety of complex indices of refraction (simulating different coals) and a variety of different particle distribution functions

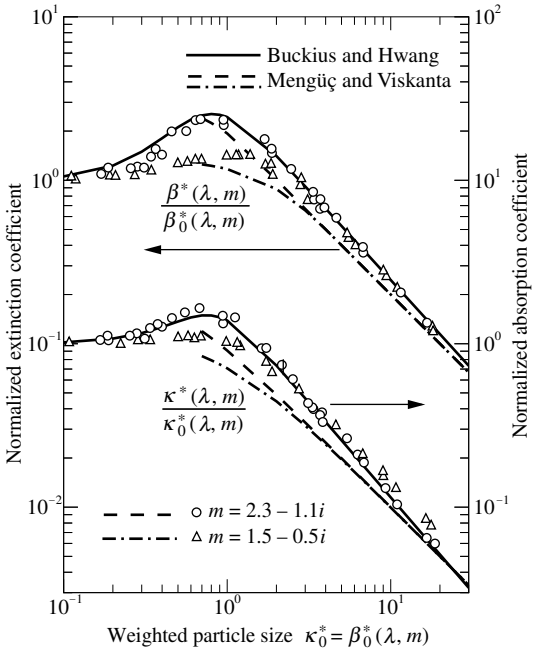

FIGURE 12-18
Extinction and absorption properties of pulverized coal [86, 87].

[gamma distributions and "rectangular" distributions, i.e., $n(a)$ = const over a certain range of radii]. They found that, when normalized with the Rayleigh small-particle limit, the absorption coefficient and extinction coefficient as well as the asymmetry factor are virtually independent of the particle size distribution function, and only depend on a mean particle diameter. Employing the range for m given by Foster and Howarth [77] for different coals, they found a similar insensitivity of the index of refraction, at least in the limits of small and large particles; in the intermediate size range, deviations of up to nearly ±50% were reported as shown in a sample of their calculations, Fig. 12-18. The spectral results were also wavelength-integrated to yield Planck-mean and Rosseland-mean absorption and extinction coefficients. Considering a temperature range of 750 K to 2500 K they found that their data could be correlated to within 30% for the different coals. Based on their numerical data for different types of coals they developed correlations for a number of nondimensional radiation properties. Spectral properties correlated were the absorption and extinction coefficients and the asymmetry factor, with nondimensional κ and β defined by

$$\kappa^*(\lambda, m) = \kappa(\lambda, m, N_T)/f_A, \quad \beta^*(\lambda, m) = \beta(\lambda, m, N_T)/f_A, \tag{12.106}$$

where

$$f_A = \int_0^\infty \pi a^2 n(a)\, da \tag{12.107}$$

is the total projected area of the particles per unit volume. Thus, these nondimensional values are essentially size-averaged absorption and extinction efficiencies [cf. equations (12.39) and (12.40)]. For extremely small particles $\kappa^* \approx \beta^*$ may be calculated from Rayleigh scattering theory, equation (12.53), as

$$\kappa_0^*(\lambda, m) = \beta_0^*(\lambda, m) = -\Im\left\{\frac{m^2 - 1}{m^2 + 2}\right\}\frac{6\pi f_v}{\lambda f_A} = -4\bar{x}\,\Im\left\{\frac{m^2 - 1}{m^2 + 2}\right\}, \tag{12.108}$$

where $\bar{x}$ is a mean size parameter based on a mean particle radius defined by

$$\bar{r} = \frac{3f_v}{4f_A} = \frac{\int_0^\infty a^3 n(a)\, da}{\int_0^\infty a^2 n(a)\, da}. \tag{12.109}$$

TABLE 12.3
Correlation parameters for the prediction of nondimensional coal properties from $y^{-z} = y_0^{-z} + y_\infty^{-z}$ [86].

y	y_0	y_∞	z
$\beta^*(\lambda, m)$	$\beta_0^*(1 + 6.78\beta_0^{*2})$	$3.09/\beta_0^{*0.1}$	1.2
$\kappa^*(\lambda, m)$	$\beta_0^*(1 + 2.30\beta_0^{*2})$	$1.66/\beta_0^{*0.16}$	1.6
$g(\lambda, m)$	g_0	0.9	1.0
β_P^*	$0.0032\phi[1 + (\phi/355)^{1.9}]$	$10.99/\phi^{0.02}$	1.2
β_R^*	$0.0032\phi[1 + (\phi/485)^{1.75}]$	$10.99/\phi^{0.02}$	1.2
κ_P^*	$0.0032\phi[1 + (\phi/725)^{1.65}]$	$13.75/\phi^{0.13}$	1.5
κ_R^*	$0.0032\phi[1 + (\phi/650)^{2.3}]$	$15.65/\phi^{0.143}$	1.15

$\phi = \bar{r}T/1\ \mu\text{m K}$, β and κ nondimensionalized by f_A from equation (12.107);
β_0^* from equation (12.108), g_0 from equation (12.110), $\bar{r}$ from equation (12.109).

Since β_0^* is linear in $\bar{x}$ it may also be regarded as a weighted (by a function of m) size parameter. The asymmetry factor for Rayleigh scattering is zero (because of its symmetric phase function) and g_0 for the small particle limit must be found from a higher-order expansion given by [86], which may be simplified to

$$g_0(\lambda, m) = \frac{1}{15}\Re\left\{\frac{(m^2+2)(m^2+3)}{2m^2+3}\right\}\left(\frac{2\pi}{\lambda}\right)^2 \frac{\int_0^\infty a^8 n(a)\,da}{\int_0^\infty a^6 n(a)\,da}. \tag{12.110}$$

In a similar fashion, they defined nondimensional Planck-mean and Rosseland-mean absorption and extinction coefficients, all normalized by f_A. All correlations obey the same basic formula,

$$\frac{1}{y^z} = \frac{1}{y_0^z} + \frac{1}{y_\infty^z}, \tag{12.111}$$

where y stands for one of the above nondimensional properties, y_0 is that property for small average particle sizes, and y_∞ the one for large average particle sizes. The correlation parameters y_0, y_∞, and z for the various properties are summarized in Table 12.3, and results of this correlation are included in Fig. 12-18. A somewhat simpler set of formulae to calculate the radiative properties in pulverized-coal reactors has been given by Kim and Lior [88].

The results of Buckius and Hwang were essentially corroborated by Viskanta and coworkers [84]. They too found that variations with particle distribution functions are relatively minor, and that the different indices of refraction made a difference only for midsized particles. However, they felt that these differences were too large to use a single correlation and presented individual graphs for different coals. Table 12.3 indicates that—according to Buckius and Hwang [86]—Planck-mean and Rosseland-mean coefficients do not depend on the optical properties of the coal and are very close to one another. Again, this observation was corroborated by Viskanta and coworkers [84] for carbon, anthracite and bituminous coal, as well as for lignite at high temperature (above 1000 K). For fly ash and for lower temperature lignite mean absorption coefficients were considerably lower due to the significantly lower absorptive indices of these materials. Thus, Table 12.3 should be regarded as a relatively crude approximation, which should be replaced when more accurate data for different coals and ashes become available (optical properties varying with wavelength and temperature, particle size distributions).

Mengüç and Viskanta [87] applied the approximate theory of equations (12.59) to two very different particle size distributions and several different complex indices of refraction (simulating carbon particles, several coals, and fly ash). They found the approximate solutions to agree very well with full Lorenz–Mie calculations, even for carbon particles [which, with $m = 2.20 - 1.12i$, significantly violate the limitations on equations (12.59)]. Like Buckius and Hwang [86] they noticed that the particle size distribution has only a very small effect on radiative properties. For comparison, results from equation (12.59) for particles of uniform size are also included in Fig. 12-18, showing good agreement with Buckius and Hwang's correlation for large particle sizes. Equations (12.59) predict the index of refraction effects more accurately but must fail for small size parameters. Liu and Swithenbank [89] used the same simplified theory, together with the comprehensive experimental data of Goodwin [83], to predict radiative properties of fly ash dispersions. They found that wavelength dependence of the complex index of refraction cannot be ignored: while n remains relatively constant, the absorptive index k of fly ash varies by orders of magnitude across the spectrum, causing large changes in radiative properties. Im and Ahluwalia [90], also using Goodwin's [83] data, have given a correlation of the complex index of refraction for fly ash, as a function of wavelength and mineral composition. Manickavasagam and Mengüç [91] gave direct correlations for the absorption coefficient of two coals (as a function of wavelength), again finding that particle size distributions did not change κ appreciably. A slightly different approach was taken by Caldas and Semião [92], who used four curve fits to the Lorenz–Mie results for Q_{ext} and Q_{sca}, covering different ranges of effective particle sizes. They applied this method to several distributions typical of fly ash and carbon particles. Small Fortran routines for the models of Buckius and Hwang and of Mengüç and Viskanta are included in Appendix F.

Radiative Properties of Soot

Soot particles are produced in fuel-rich flames, or fuel-rich parts of flames, as a result of incomplete combustion of hydrocarbon fuels. As shown by electron microscopy, soot particles are generally small and spherical, ranging in size between approximately 50 Å and 800 Å (5 nm to 80 nm), and up to about 3000 Å in extreme cases [93, 94]. While mostly spherical in shape, soot particles may also appear in agglomerated chunks and even as long agglomerated filaments. It has been determined experimentally in typical diffusion flames of hydrocarbon fuels that the volume percentage of soot generally lies in the range between 10^{-4}% to 10^{-6}% [76, 95, 96].

Since soot particles are very small, they are generally at the same temperature as the flame and, therefore, strongly emit thermal radiation in a continuous spectrum over the infrared region. Experiments have shown that soot emission often is considerably stronger than the emission from the combustion gases. In order to predict the radiative properties of a soot cloud, it is necessary to determine the amount, shape, and distribution of soot particles, as well as their optical properties, which depend on chemical composition and particle porosity. It is known today that key steps in soot formation and destruction (oxidation) are [97–105]: formation of gas-phase precursors (polycyclic aromatic hydrocarbons—PAHs) in fuel-rich regions; soot particle inception ($\sim$ 1 nm particle size); particle surface growth involving acetylene (C_2H_2) and/or PAHs; particle coagulation/agglomeration (up to tens of μm particle size); and oxidation in oxygen-rich regions. High-level soot models often employ concentration moments of the soot distribution function [106–108]: this "method-of-moments" has the advantage that it allows the distribution of soot particles to be computed using essentially the same approach that is used for gas-phase chemical species.

Early work on soot radiation properties concentrated on predicting the absorption coefficient κ_λ for a given flame as a function of wavelength. For all but the largest soot particles the size parameter $x = 2\pi a/\lambda$ is very small for all but the shortest wavelengths in the infrared, so one may expect that Rayleigh's theory for small particles will, at least approximately, hold. This condition would, according to equation (12.53), lead to negligible scattering and an absorption

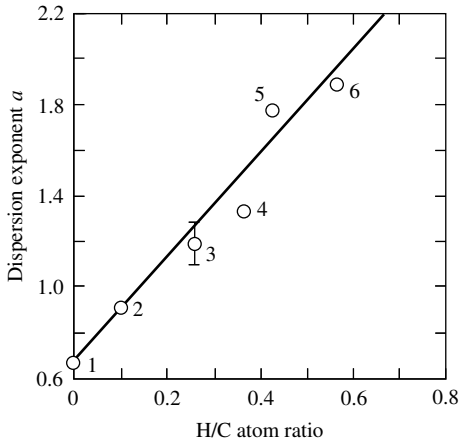

FIGURE 12-19
Dispersion exponent a of soot deposits *vs.* hydrogen-to-carbon ratio: 1, pure carbon (arc evaporated); 2, acetylene/oxygen flame; 3, ethylene/oxygen flame; 4, 5, 6, ethylene/air flames [110].

coefficient of

$$\kappa_\lambda = \beta_\lambda = -\mathfrak{I}\left\{\frac{m^2-1}{m^2+2}\right\}\frac{6\pi f_v}{\lambda} = \frac{36\pi nk}{(n^2-k^2+2)^2+4n^2k^2}\frac{f_v}{\lambda}. \tag{12.112}$$

In the soot literature it is common to employ a (soot) "refractive index function,"

$$E(m) = -\mathfrak{I}\left\{\frac{m^2-1}{m^2+2}\right\} = \frac{6nk}{(n^2-k^2+2)^2+4n^2k^2} \tag{12.113}$$

and the absorption coefficient reduces to

$$\kappa_\lambda = \beta_\lambda = 6\pi E(m)\frac{f_v}{\lambda}. \tag{12.114}$$

Experiments have confirmed that scattering may indeed be neglected [109]. The form of equation (12.114) would lead one to expect that the absorption coefficient should vary with wavelength as $1/\lambda$. However, this assumption is only approximately correct, since the complex index of refraction m (and, in particular, the absorptive index k) can vary significantly across the spectrum. It is customary to write

$$\kappa_\lambda = \frac{Cf_v}{\lambda^a}, \tag{12.115}$$

where C and a are empirical constants. Many different values for the *dispersion exponent* a have been measured by investigators for many different flame conditions, ranging from as low as 0.7 to as high as 2.2. Earlier theories explained this deviation from Rayleigh theory to be a consequence of particle size. While it is true that Lorenz–Mie theory predicts a growing value for a for increasing particle size, it is easy to show that this alone cannot explain the large values for the dispersion exponent in some flames. Rather, this increase in a must be due to spectral variations of the effective complex index of refraction, resulting from the chemical composition and the porosity of the soot particles. Millikan [110,111] investigated the dependence between dispersion exponent and chemical composition. While for many years soot was assumed to be amorphous carbon, he found the particles contained considerable amounts of hydrogen (up to 40 atom-%), and he determined that a was approximately directly proportional to the hydrogen–carbon ratio of the soot material as shown in Fig. 12-19. He further showed that the radiative properties of the soot were the same for in situ flame measurements as for soot collected from the flame, suggesting that the optical properties are fairly independent of temperature. Unfortunately, his experimental setup did not allow for the determination of the constant C in equation (12.115), so that quantitative evaluation of the extinction coefficient is not possible.

The optical properties of soot material, i.e., the complex index of refraction m, have received a very considerable amount of attention during the last forty years, using different forms of carbon and various experimental methods. Foster and Howarth [77] were the first to report experimental measurements for the complex index of refraction of hydrocarbon soot, based on various carbon black powders. This work was followed shortly thereafter with measurements by Dalzell and Sarofim [112] on soot collected on cooled brass plates from laminar diffusion flames burning either acetylene or propane. In both cases pellets with very smooth, quasi-specular surfaces were formed by compressing small soot samples between optically flat surfaces with pressures up to 2760 bar. The index of refraction was then deduced from reflectance measurements employing Fresnel's relations for specular reflectors. They found the optical properties of the two different soots to be fairly similar, with values for acetylene soot somewhat higher than for propane soot, apparently because of the higher H/C ratio in propane soot. Comparing their results with values reported by Stull and Plass [113] (based on amorphous carbon) and by Howarth, Foster, and Thring [114] (based on pyrographite) they note that optical properties of amorphous or graphitic carbon are not equal to those of soot, primarily because of the different H/C ratios.

The data of Dalzell and Sarofim [112] have been employed in many subsequent studies (and continue to be used today). For example, Hubbard and Tien [115] used them to evaluate Planck-mean and Rosseland-mean absorption coefficients for soot clouds and soot–gas mixtures. However, the accuracy of Dalzell and Sarofim's data has been questioned by a number of researchers. All ex situ measurements suffer from the fact that during the analysis the soot is not in the same state as in the flame. The soot particles are at a different temperature, and they may have different morphologies because of agglomeration during the sampling process. The severest criticism concerns the pellet-reflection technique. Medalia and Richards [116], Graham [117], and Janzen [118] have pointed out that the pellets must contain a considerable amount of void (33% even after compression to 2760 bar, according to Medalia and Richards [116]), since the sample is made by compressing a powder. This technique leads to two serious sources for errors: (*i*) Since the pellets are actually a two-phase dispersion of soot and air, the inferred index of refraction is the one of the dispersion and not the one of the soot particles themselves, and (*ii*) at least at short wavelengths the pellet cannot be assumed to be optically smooth and Fresnel's relations become invalid.

These problems prompted Lee and Tien [119] to obtain soot optical properties from in situ flame transmission data together with application of the *dispersion theory* [18,120] (i.e., the theory that predicts the wavenumber dependence of the optical constants n and k by relating them to bound- and free-electron densities). Their results for polystyrene and Plexiglas flame soot, based on data by Buckius and Tien [121] and Bard and Pagni [122], are shown in Fig. 12-20 together with the data of Stull and Plass [113], Howarth and coworkers [114], and the propane soot results of Dalzell and Sarofim [112] and Chang and Charalampopoulos [123]. Lee and Tien's data agree fairly well with those of Dalzell and Sarofim, except for the visible where the pellet-reflection technique is particularly suspect. In contrast to Dalzell and Sarofim as well as Millikan [110, 111], Tien and Lee noted that the optical properties varied little from flame to flame despite their different fuel (not necessarily soot) H/C ratios. Conceivably the soot of their different flames had similar H/C ratios. They also applied the dispersion theory to determine the temperature dependence of the optical properties, observing that $m = n - ik$ is very insensitive to temperature changes at high temperature levels. This would imply negligible effect of spatial temperature variation on soot properties, as is commonly assumed. It should be noted that, like the pellet-reflection technique, the spectral transmission technique has its own set of difficulties: For its data reduction, a scattering theory and a theory describing the spectral variation of the refractive index (the dispersion theory) must be used. Usually the Lorenz–Mie scattering theory based on monodisperse spherical soot particles is employed. Thus, only when the particles are spherical with a single diameter can these results be used with confidence. The more recent data of Chang and Charalampopoulos show similar values for the refractive index, but somewhat

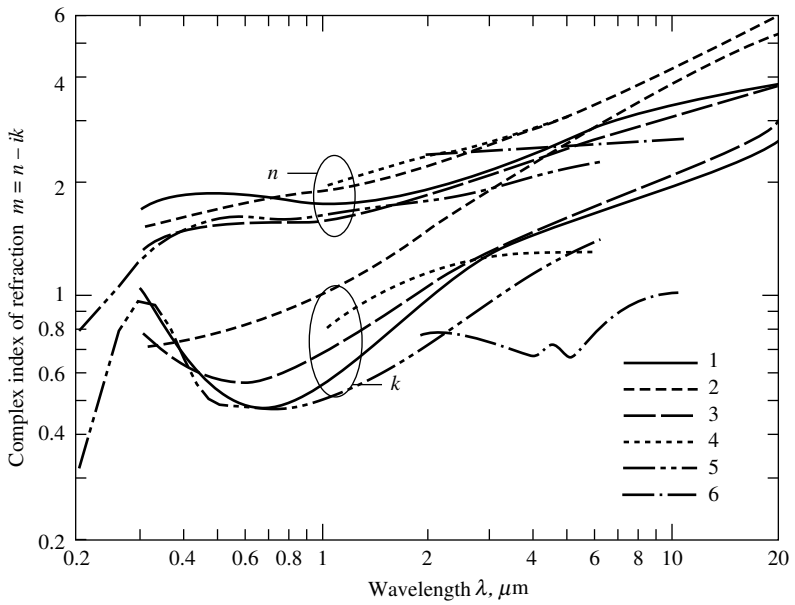

FIGURE 12-20
Complex index of refraction for soot based on different studies: 1, Lee and Tien [119] (polystyrene and Plexiglas soot); 2, Stull and Plass [113] (amorphous carbon); 3, Dalzell and Sarofim [112] (propane soot); 4, Howarth and coworkers [114] (pyrographite at 300 K); 5, Chang and Charalampopoulos [123] (propane soot); 6, Felske and coworkers [125] (propane soot).

lower absorptive indices. Their data have been confirmed in even more recent studies covering diverse flame conditions [124]. Chang and Charalampopoulos [123] also provided a polynomial expression, valid for the wavelength range

$$0.4\,\mu\text{m} \le \lambda \le 30\,\mu\text{m}:$$

$$n = 1.811 + .1263\ln\lambda + .0270\ln^2\lambda + .0417\ln^3\lambda, \tag{12.116a}$$

$$k = .5821 + .1213\ln\lambda + .2309\ln^2\lambda - .0100\ln^3\lambda, \qquad \lambda \text{ in } \mu\text{m}. \tag{12.116b}$$

In another investigation Felske and coworkers [125] returned to the pellet-reflection technique, arguing that—for a carefully prepared pellet—the data in the infrared do obey Fresnel's relations. They also measured the void fraction over the first few layers of particles (where all absorption occurs) and found that the proportion of voids in these layers is significantly lower (18%) than in the bulk of the material (33%). For their data evaluation they first determined the applicability of Fresnel's relations by measuring the *specularity index* defined as

$$s = \rho_\perp^2\left(\frac{\pi}{4}\right)\Big/\rho_\parallel\left(\frac{\pi}{4}\right), \tag{12.117}$$

where $\rho_\perp$ and $\rho_\parallel$ are the perpendicular and parallel polarized components of the pellet reflectance, respectively. For a surface obeying Fresnel's relations $s \equiv 1$ always, regardless of the complex index of refraction of the material [cf. equations (3.52) and (3.53)]. They determined that their surfaces could be considered specular reflectors for wavelengths $\lambda \ge 2.0\,\mu$m. They then proceeded to correct their data for the measured void fraction using a number of different models. Their data for the refractive index of propane soot are also included in Fig. 12-20. Their data, even after correction for voidage (which raises the value for n by approximately 0.3, and for k by approximately 0.15), differ significantly from those of other investigations and depend only weakly on wavelength.

It is well known today that in most flames soot particles agglomerate into large chunks or long chains, making the use of the spherical-particle assumption very questionable. A

number of textbooks have considered scattering by nonspherical particles [3, 16, 18], and a short introduction to methods for nonspherical particles and agglomerates was provided in Section 12.10. Approximating chunks of soot as prolate spheroids, Jones [126] found their absorption behavior to be considerably different from that of spheres of identical volumes. Lee and Tien [127] investigated the extreme case of long chains approximated by infinite cylinders. They found that the extinction coefficient for spheres drops off in the infrared much faster than the one for cylinders of the same radius. However, the wavelength-integrated extinction coefficient is rather insensitive to particle shape at elevated temperatures, say $T > 1000\,\mathrm{K}$ (i.e., at flame temperatures where soot emission may be important) [127]. Similar results were found by Mackowski and coworkers [128], who looked at infinite soot cylinders also using Lee and Tien's optical properties. Investigating the behavior of polydisperse cylindrical soot particles, they found the behavior to be similar to that observed by Buckius and Hwang [86] for polydisperse coal particles. While they generated correlations for absorption and extinction coefficients according to equation (12.111), unfortunately their correlation is rather cumbersome to use since different sets of parameters apply to each of a large number of wavelengths.

In more modern measurements Dobbins and Megaridis [129] built a thermophoretic probe that made it possible to sample soot aggregates from flames for electron microscope studies. They showed that near the start of soot formation small aggregates form (on the order of 10 nm), while clusters up to 1 μm in length can be found in turbulent flames, i.e., sizes clearly too large for the Rayleigh theory to hold. Experiments have further shown that soot aggregates resemble mass fractals, and the number of soot particles in an aggregate is given by[3]

$$N = k_f (R_g/a)^{D_f}, \tag{12.118}$$

where a is the radius of the individual soot particles, R_g is the radius of gyration, and D_f and k_f are mass fractal dimension and fractal prefactor, respectively [130, 131]. Various soot aggregates of different size and shape have been found to have universal morphology with $1.6 < D_f < 1.9$ and $2.0 < k_f < 2.6$, almost independent of fuel or position within a flame [132–135]. On the other hand, fractal clusters generated theoretically by *diffusion limited cluster aggregation* (DLCA) tend to lead to smaller fractal prefactors of around 1.2 [136], a discrepancy that remains unresolved. For monodisperse particles the radius of gyration is found from

$$R_g^2 = \frac{1}{N} \sum_{i=1}^{N} r_i^2, \tag{12.119}$$

where r_i is the distance from the center of each particle to the center of gravity of the soot aggregate.

Accordingly, more recent theoretical studies have modeled agglomerated soot as long chains of spherical particles [133, 137–155]. Three different fundamental approaches have been pursued, most using Jones' formulation [156, 157], which in turn is based on Saxon's integral equation [158]. In this method primary soot particles are assumed to obey Rayleigh scattering and the electric field inside them is taken as uniform, while the field outside the particles is determined from the integral representation of Maxwell's equations [137–142]. In the discrete dipole approximation (DDA) of Purcell and Pennypecker [73] the soot aggregate is modeled as an array of N polarizable elements ("dipoles") in vacuum, leading to a set of linear algebraic equations [143–146]. In the model of Iskander and coworkers [159], known as the I-C-P model, the aggregate is divided into cubical or spherical cells with uniform electromagnetic fields. A control volume analysis converts the governing equations to a set of linear algebraic ones [147–149]. Results from these aggregate models show that approximating agglomerated soot as infinitely long cylinders [127, 128] leads to significant errors. In recent years a number

[3] In the early work of Dobbins and Megaridis [129], as well as in some later papers, equation (12.118) was based on primary particle diameter, $2a$, which increases k_f by a factor of 2^{D_f}, while most authors today use the form given here.

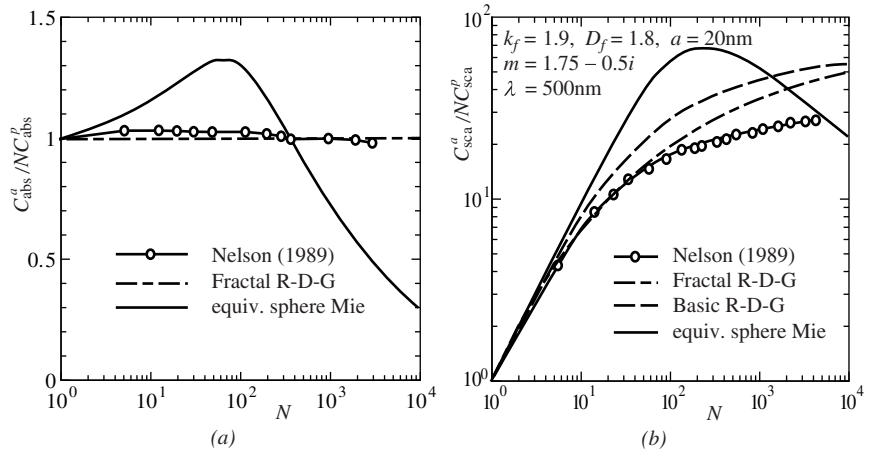

FIGURE 12-21
Absorption and scattering cross-sections of soot aggregates (C^p is cross-section for a single particle, C^a for an aggregate, and N is the number of soot particles in the aggregate) [151].

of numerically exact (and computer intensive) simulations of fractal soot aggregates have also been carried out, using the T-matrix and generalized multisphere Mie (GMM) solutions, as briefly described in Section 12.10 [59,61,69–71,160,161].

Good reviews of the different methods to calculate scattering properties of agglomerated soot have been given by Köylü and Faeth [151], Manickavasagam and Mengüç [154], and by Sorensen [162], also assessing a number of more approximate theories, such as regular Rayleigh scattering (treating particles as independent), equivalent-sphere Mie scattering (replacing the agglomerate by a single sphere of equal volume), and Rayleigh–Debye–Gans (R-D-G) scattering (valid for $|m-1| \ll 1$) for both assumed shapes (such as straight chains) as well as fractal aggregates. While Rayleigh scattering always underpredicts scattering, equivalent-sphere Mie scattering can give acceptable results under certain conditions, in particular for small aggregates, but must also be regarded as unreliable, in general. The R-D-G scattering theory tends to give relatively good results, especially if fractal aggregates are considered (i.e., conforming to experimental observations). However, the R-D-G scattering theory assumes a complex index of refraction near unity, which is clearly not very accurate for soot, especially at larger wavelengths (see Fig. 12-20). Köylü and Faeth [163] pointed out and corrected inconsistencies in the fractal R-D-G model of Dobbins and Megaridis [150], as reported in [151], and revised results have been given by Farias and coworkers [152]. Another variation of the R-D-G approach has been reported by Sorensen and Roberts [136], using a slightly different form factor. Zhao and Ma [61] have compared the two R-D-G models and assessed their accuracy, finding both models to perform about equally well.

Results from equivalent-sphere Mie calculations and R-D-G calculations are compared with approximate I-C-P calculations of Nelson [147] (assuming a mean scalar field) in Fig. 12-21 [151]. Figure 12-21*a* shows that the absorption cross-section of a soot aggregate, C^a_{abs}, differs by only a few percent from that of N independent soot particles. This result is also obtained by the R-D-G theory (for assumed or fractal aggregates) since it neglects agglomeration effects on absorption, while the equivalent sphere calculations become totally unreliable for $N > 10$. Mackowski [164] used the *electrostatic approximation* (ESA) to calculate C^a_{abs} for fractal aggregates with various indices of refraction. He found that agglomeration effects on the absorption coefficient are well correlated by

$$\left(\frac{C^a_{abs}}{NC^p_{abs}}\right) = \frac{3}{2N+1} + \frac{2(N-1)}{2N+1}\left(\frac{C^a_{abs}}{NC^p_{abs}}\right)_\infty, \tag{12.120}$$

with the limiting value for $N \to \infty$ depending on the refractive index function $E(m)$. For typical soot optical constants $(C^a_{abs}/NC^p_{sca})_\infty$ is relatively small (= 1.06 for $m = 1.6 - 0.6i$), but can be substantial for larger m. These results were qualitatively confirmed by Liu and Smallwood [69, 70], who used the exact GMM formulation. However, they noted that C^p_{abs} also depends on primary particle size, and that equation (12.120) becomes inaccurate for large soot particles ($x > 0.1$).

Figure 12-21*b* indicates that the relative scattering cross-section, C^a_{sca}/NC^p_{sca}, strongly increases with particle number—first linearly (for small aggregates with negligible multiple scattering and self-interaction), then tending toward a saturation value for large N. Again, the equivalent sphere predictions become unreliable for $N > 10$ or so, while the R-D-G model gives plausible results, especially if the same fractal distribution as that of Nelson is used. The fractal R-D-G results in Fig. 12-21*b* reflect the corrections made by Köylü and colleagues [152, 163], which leads to a large-agglomerate limit for the scattering cross-section of

$$\left(\frac{C^a_{sca}}{NC^p_{sca}}\right)_\infty = \frac{k_f}{(2x)^{D_f}}\left[\frac{3}{2-D_f} - \frac{12}{(6-D_f)(4-D_f)}\right], \tag{12.121}$$

while for intermediate values of N the data of Farias and coworkers [152] are accurately correlated by a simple power law,

$$\frac{C^a_{sca}}{NC^p_{sca}} = \left(\frac{C^a_{sca}}{NC^p_{sca}}\right)_\infty^{1-N^{-1/4}}. \tag{12.122}$$

Agreement between R-D-G results and Nelson's I-C-P model is good except for large clusters, for which Nelson's results have been shown to underpredict the relative scattering cross-section by the more complete I-C-P calculations of Farias and coworkers [152]. Comparison with exact GMM calculations of Liu and Smallwood [70] showed good agreement with equation (12.122) for all N. Recent measurements of Chakrabarty [135] on ethene soot, determining absorption and scattering coefficients via nephelometry and photoacoustic spectroscopy, produced a fractal prefactor of $k_f = 2.6$, and a mass fractal dimension of $D_f = 1.7$. Comparison with R-D-G theory showed the results to be always within 10%. While perhaps not yet established as a completely reliable tool, it is generally agreed today that the fractal R-D-G theory provides simple and reliable estimates of the radiative properties of agglomerated soot.

All of the above models assume soot aggregates to consist of single size and spherical primary particles. Extensive measurements by Dobbins and Megaridis [129] and by Köylü and colleagues [132, 165] have shown that soot primary particles generally vary in size between 15 and 50 nm, depending on fuel and on flame location, but that their local size distribution has indeed a very small standard deviation (almost uniform). The number of particles comprising an aggregate, N, on the other hand, shows strong local and global variations, following a log-normal distribution with geometric standard deviations ranging from 2 to 3.5.

For a simplified heat transfer analysis it is generally desirable to use suitably defined mean absorption and extinction coefficients such as the Planck-mean and Rosseland-mean. If the soot particles are very small so that the Rayleigh theory applies for all particles and relevant wavelengths, then the extinction coefficient is described by equation (12.114). By choosing appropriate spectral average values for the refractive index n and absorptive index k one may approximate the extinction coefficient by

$$\kappa_\lambda = \beta_\lambda = C_0 \frac{f_v}{\lambda}, \quad C_0 = 6\pi E(m_{avg}) = \frac{36\pi nk}{(n^2-k^2+2)^2 + 4n^2k^2}, \tag{12.123}$$

where C_0 is now a constant depending only on the soot index of refraction. With this simple $1/\lambda$ wavelength dependence, Planck-mean and Rosseland-mean extinction coefficients are readily calculated as

$$\kappa_P = \beta_P = 3.83 f_v C_0 T/C_2, \quad \kappa_R = \beta_R = 3.60 f_v C_0 T/C_2, \tag{12.124}$$

where $C_2 = 1.4388\,\text{cm K}$ is the second Planck function constant. It is interesting to note that the Planck-mean coefficient (appropriate for optically thin situations) differs by only 6% from the Rosseland-mean (appropriate for optically thick situations). Thus, Felske and Tien [166] have suggested using an average value of

$$\kappa_m = \beta_m = 3.72 f_v C_0 T / C_2 \tag{12.125}$$

for all optical regimes. It is important to keep in mind that the above formulae apply only to very small soot particles, and that the extinction coefficient will increase for aggregates, as indicated in Fig. 12-21, or if primary particle sizes are encountered that exceed Rayleigh scattering limits.

Example 12.4. Propane is burned with air under fuel-rich conditions, resulting in a volume fraction of soot of $f_v = 10^{-5}$. Determine the extinction coefficient for very small particles at a wavelength of 3 μm using the refractive index data of (*i*) Lee and Tien, (*ii*) Stull and Plass, (*iii*) Dalzell and Sarofim, (*iv*) Chang and Charalampopoulos, and (*v*) Felske and coworkers. If the soot consisted of long fractal aggregates with 100 soot particles each ($a = 50\,\text{nm}$), how would the extinction coefficient change?

Solution

To determine the extinction coefficient for small spherical soot particles we use equation (12.112) together with optical property data from Fig. 12-20:

Lee and Tien:	$n = 2.21$,	$k = 1.23$,	$\kappa_\lambda = 0.1754\,\text{cm}^{-1}$;
Stull and Plass:	$n = 2.63$,	$k = 1.95$,	$\kappa_\lambda = 0.1472\,\text{cm}^{-1}$;
Dalzell and Sarofim:	$n = 2.19$,	$k = 1.30$,	$\kappa_\lambda = 0.1835\,\text{cm}^{-1}$;
Chang and Charalampopoulos	$n = 1.89$,	$k = 0.92$,	$\kappa_\lambda = 0.1904\,\text{cm}^{-1}$;
Felske and coworkers:	$n = 2.31$,	$k = 0.71$,	$\kappa_\lambda = 0.1077\,\text{cm}^{-1}$.

Thus, the values found from the data of Lee and Tien, Dalzell and Sarofim, and Chang and Charalampopoulos are fairly consistent, while the absorptive index based on Stull and Plass' data is considerably higher, probably because amorphous carbon simply does not represent soot well. The absorptive index based on the data of Felske and coworkers is by far the lowest. The extinction coefficient for soot aggregates can be estimated from equation (12.122). Reworking Example 12.1 (i.e., using Lee and Tien's data, but with ten times the volume fraction and twice the particle size), we find $x = 2\pi \times 0.05/3 = 0.1048$, $Q^p_{\text{abs}} = 1.17 \times 10^{-1}$, and $Q^p_{\text{sca}} = 1.94 \times 10^{-4}$. For an aggregate, the absorption coefficient remains relatively unchanged. If we employ equation (12.120) with $(C^a_{\text{abs}}/NC^p_{\text{sca}})_\infty \simeq 1.06$, we obtain

$$\left(\frac{C^a_{\text{sca}}}{NC^p_{\text{sca}}}\right) = \frac{3}{201} + \frac{2 \times 99}{201} \times 1.06 \simeq 1.06,$$

i.e., the absorption coefficient increases by about 6%, or

$$\kappa_\lambda = Q^a_{\text{abs}} \pi a^2 (N_T/N) = \left(C^a_{\text{abs}}/NC^p_{\text{abs}}\right) Q^p_{\text{abs}} \pi a^2 N_T = \left(C^a_{\text{abs}}/NC^p_{\text{abs}}\right) Q^p_{\text{abs}} \frac{3 f_v}{4a}$$
$$= 1.06 \times 0.117 \times \frac{3 \times 10^{-5}}{4 \times 5 \times 10^{-6}\,\text{cm}} \simeq 0.1860\,\text{cm}^{-1}.$$

On the other hand, the scattering coefficient becomes (using the fractal parameters of Fig. 12-21)

$$\sigma_{s\lambda} = Q^a_{\text{sca}} \pi a^2 (N_T/N) = \left(C^a_{\text{sca}}/NC^p_{\text{sca}}\right) Q^p_{\text{sca}} \frac{3 f_v}{4a}$$
$$\left(\frac{C^a_{\text{sca}}}{NC^p_{\text{sca}}}\right)_\infty = \frac{1.9}{(2 \times 0.1048)^{1.8}} \left[\frac{3}{0.2} - \frac{12}{4.2 \times 2.2}\right] = 433.5$$
$$\frac{C^a_{\text{sca}}}{NC^p_{\text{sca}}} = 433.5^{1-100^{-1/4}} = 63.5$$

and

$$\sigma_{s\lambda} \simeq 63.5 \times 1.94 \times 10^{-4} \times \frac{3 \times 10^{-5}}{4 \times 5 \times 10^{-6}\,\text{cm}} \simeq 1.85 \times 10^{-2}\,\text{cm}^{-1}.$$

Adding together we find $\beta_\lambda = \kappa_\lambda + \sigma_{s\lambda} = 0.1860 + .0185 = 0.2045\,\text{cm}^{-1}$, i.e., while scattering from aggregates is 63 times larger than that from individual particles, and may not be negligible (depending on the physical size of the soot cloud), its impact on the extinction coefficient is fairly small.

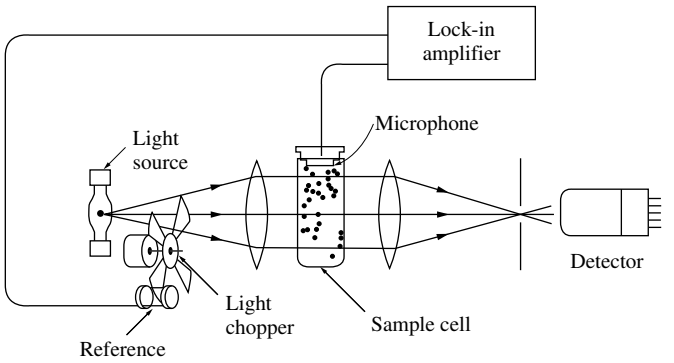

FIGURE 12-22
Schematic for measurement of extinction coefficient and absorption coefficient [18].

12.12 EXPERIMENTAL DETERMINATION OF RADIATIVE PROPERTIES OF PARTICLES

Experimental measurements of radiative properties of particles and clouds of particles are useful to verify the Lorenz–Mie theory, to ascertain the applicability of the Lorenz–Mie theory (for nonspherical particles, nonisotropic particles, closely spaced particles, etc.), or simply to determine the radiative properties of particles for which no theory exists. A comprehensive review of such experiments up to 1991 has been given by Agarwal and Mengüç [167]. Properties that can be measured are *extinction coefficient*, *absorption coefficient*, and *scattered intensity*. The easiest property to measure is the *extinction coefficient*. In principle, a standard spectrometer can be used for this measurement. The results, however, may be unreliable unless the detector is modified to eliminate forward-scattered light, which may account for the majority of total extinction [18] (in particular for large particle sizes, cf. Figs. 12-6 and 12-7). A schematic of such an apparatus is shown in Fig. 12-22. Light from a point source is collimated by a lens, transmitted through the sample cell (with its suspension of particles), and then focused onto a detector by a second lens. In order to reject forward-scattered light, the detector is covered by a guard plate with a small pinhole located at the focal point of the second lens. The diameter of the pinhole must be carefully optimized: If the hole is too small then the signal from the transmitted light may become too weak, while a hole too large will admit an unacceptable amount of forward-scattered energy to the detector. Normally the light beam is chopped by a rotating blade since most detectors only respond to *changes* in irradiation.

To distinguish between absorption and scattering, either the absorption coefficient or total scattering must be measured independently. To measure scattering over all (forward and backward) directions is very difficult, requiring a spectrometer capable of collecting radiation going into all directions (usually accomplished with an integrating sphere technique described in Chapter 3; cf., for example, Bryant *et al.* [168]). Absorption can also be detected fairly easily with a method usually referred to as *photoacoustic* [18]. Particles irradiated by a chopped beam are heated periodically, causing periodic changes in the particle temperature, which in turn cause slight pressure oscillations that may be detected by a sensitive microphone. These signals are then amplified by a lock-in amplifier synchronized with the light chopper. Since only absorbed light causes a temperature change in the particles, the acoustic signal must be proportional to the absorption coefficient of the suspension. Details may be found in the papers by Roessler and Faxvog [169] and Faxvog and Roessler [170], who measured the absorption coefficients of acetylene smoke and diesel emissions using this method. An ingenious way to separate transmitted and scattered radiation in the visible has been developed by Härd and Nilsson [171], who utilized the Doppler effect that occurs when an electromagnetic wave is scattered by a moving particle.

Angular scattering measurements are carried out with a *scattering photometer* (sometimes

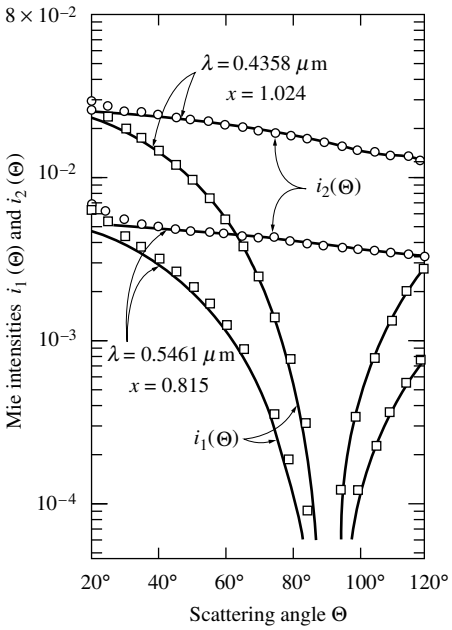

FIGURE 12-23
Lorenz–Mie scattering intensities i_1 and i_2 for 0.106 μm diameter spheres; data points experimental, solid lines theoretical [172].

called a *nephelometer*). We distinguish between measurements with *single scattering* (i.e., the cell contains a dilute particle mixture that is optically thin, $\sigma_s L \ll 1$, so that every light beam is scattered at most once before exiting the particle layer) and *multiple scattering*, between *monodisperse suspensions* (i.e., all particles are exactly the same size) and *polydisperse suspensions* (i.e., the particle sizes obey a certain distribution function), between *near-forward scattering* (to measure the strong forward-scattering peak, but separating it from transmission) and scattering into all directions. Angular light scattering measurements are sometimes classified as either *absolute* or *relative*. In an absolute measurement the ratio between intercepted and scattered radiation, $\delta I_s(\Theta)/I_i$, is measured directly, while in a relative measurement the scattered intensity is related to intensity scattered into a reference direction, $\delta I_s(\Theta)/\delta I_s(\Theta_{\text{ref}})$. Thus neither measurement is truly "absolute"; in both cases a relative (i.e., nondimensional) intensity is recorded [18]. Since relative measurements are considerably easier to make, this method is employed by most experimentalists.

Single scattering experiments have been carried out primarily to verify the Lorenz–Mie theory, or to assess the accuracy of a device to be used for other scattering measurements. Hottel and coworkers [172] described such an experiment, in which they measured the nondimensional polarized intensities given by equation (12.10) for monodisperse polystyrene latex spheres (it appears that polystyrene spheres are favored by most experimenters, since it is relatively easy to manufacture spheres of constant diameter and of known index of refraction in the visible, $m = 1.60$, i.e., the spheres scatter but do not absorb). Their equipment consisted of a mercury arc and optics to produce an unpolarized near-parallel beam, a polarizer, a test cell manufactured from parallel microscope slides, and optics to confine the received beam to a small divergence angle. Their results for single scattering of small ($2a = 0.106\ \mu$m) spheres are shown in Fig. 12-23. It is seen that the agreement between experiment and Lorenz–Mie theory is excellent. Hottel and coworkers attribute the small discrepancies primarily to the unavoidable spread in particle sizes. A more modern device to measure the scattering phase function for (almost) single scattering, as well as extinction and scattering coefficients, has been reported by Menart and colleagues [173]. Their apparatus employed a globar light source and an open gas-particle column, both mounted on a rotatable table, together with collection optics and a highly sensitive dual element (InSb–HgCdTe) detector. Measurements taken for soda–lime glass beads

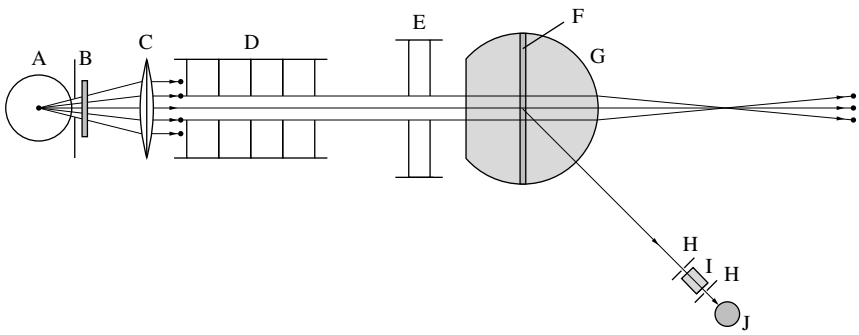

FIGURE 12-24
Schematic for angular scattering experiment [177]: A, Hg arc; B, monochromatic filter; C, lens; D, E, H, light stops; F, test section; G, jacket with Nujol; I, analyzer; J, photomultiplier.

and aluminum oxide particles in the wavelength range between 2.5 and 11 μm showed good agreement with Lorenz–Mie theory.

Multiple scattering experiments were reported by Woodward [174,175], also on polystyrene spheres, using dispersions with narrow size distribution. Woodward found good agreement between his data and the multiple-scattering theory of Hartel [176], a somewhat dated approximate solution of the equation of transfer for a purely scattering medium. However, as Smart and coworkers [177] pointed out, Woodward did not correct for the reflection of the emergent beam at the water–glass–air interfaces of the test cell, nor did he account for the change in scattering path length for larger angles. To compensate for these errors, Smart and coworkers [177] devised an apparatus whose schematic is shown in Fig. 12-24. Employing a standard Brice–Phoenix spectrometer, they placed the simple parallel-microscope slide test section inside a special cell filled with Nujol (a liquid paraffin). Nujol has the same refractive index as the glass bounding the test section as well as the outer jacket of the cell. Thus, the Nujol serves two purposes: Reflections at the interfaces are almost eliminated and—from Snell's law—all scattering angles up to 90° are contained in experimental angles below 65°, making otherwise impossible-to-measure scattering angles measurable. Some representative results of their multiple-scattering measurements for varying optical thicknesses of the particle suspension are shown in Fig. 12-25. Agreement between experiment and theory is excellent except for very small and very large optical thicknesses. For small thicknesses the experiment could not regenerate the maxima and minima, probably as a result of uncertainty in the particle size distribution. Disagreement for large thicknesses stems from the fact that Smart and coworkers also used Hartel's approximate theory. Orchard [178] pointed out that using Hartel's approximation leads to a transmissivity of 0.5 for a medium of infinite optical thickness (rather than the correct value of zero). Therefore, Hottel and coworkers [172] used the method of discrete ordinates, which may be made arbitrarily accurate for sufficient numbers of "ordinates,"[4] to calculate bidirectional reflectance and transmissivity for a particle layer. Some representative data in Fig. 12-26 show the excellent agreement between theory and experiment for optical thicknesses up to 775. Very similar experiments, also using the method of discrete ordinates for theoretical calculations, were carried out by Brewster and Tien [5] and Yamada, Cartigny, and Tien [6] for large polydivinyl spheres in air, resulting in equally good agreement between experiment and theory. A different approach to avoiding reflection and refraction losses, and to measuring scattering intensities at oblique angles, was taken by Daniel and coworkers [179], who measured the phase function for aqueous suspensions of unicellular algae. They used a rotatable fiber-optic detector immersed *inside* the large dish filled with a dilute algae suspension.

Measurements of the radiative properties of soot have become important for a number of reasons. For one, soot is a very strong radiator and more often than not dominates the heat

[4]This method for the solution of the radiative transport equation is described in detail in Chapter 17.

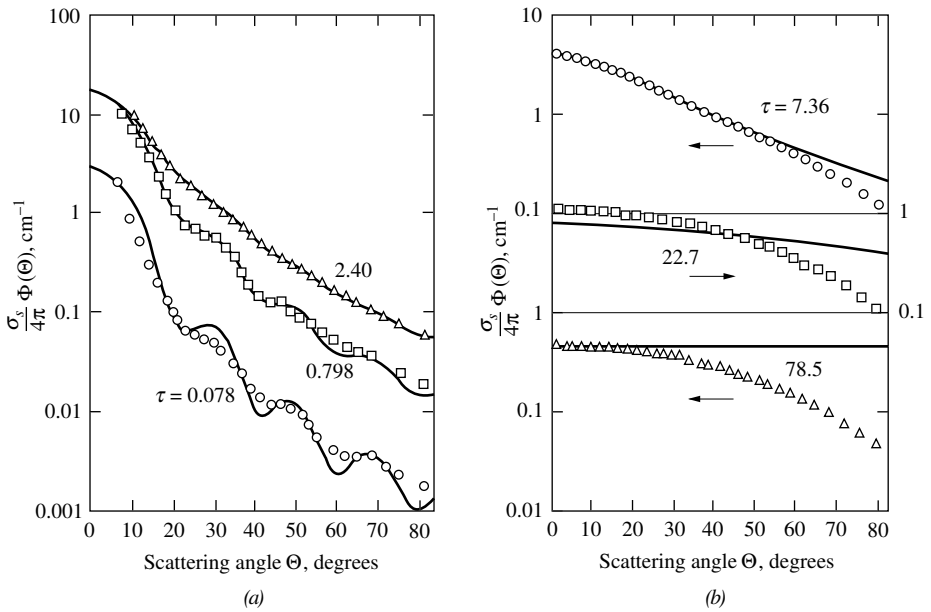

FIGURE 12-25
Relative scattered intensity *vs.* angle of observation *(a)* for relatively low concentration, *(b)* for relatively high concentration; data points experimental, solid lines theoretical [177].

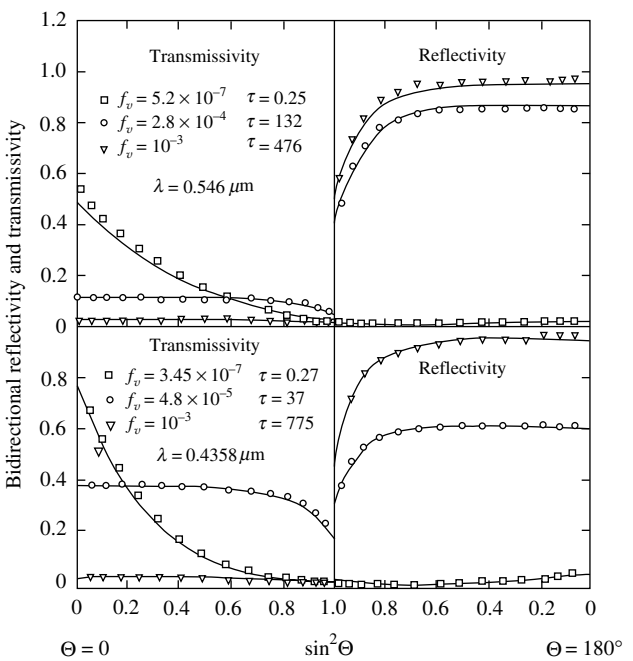

FIGURE 12-26
Bidirectional reflectance and transmissivity of an aqueous solution of 0.530 μm polystyrene spheres, for varying concentrations; data points experimental, solid lines theoretical [172].

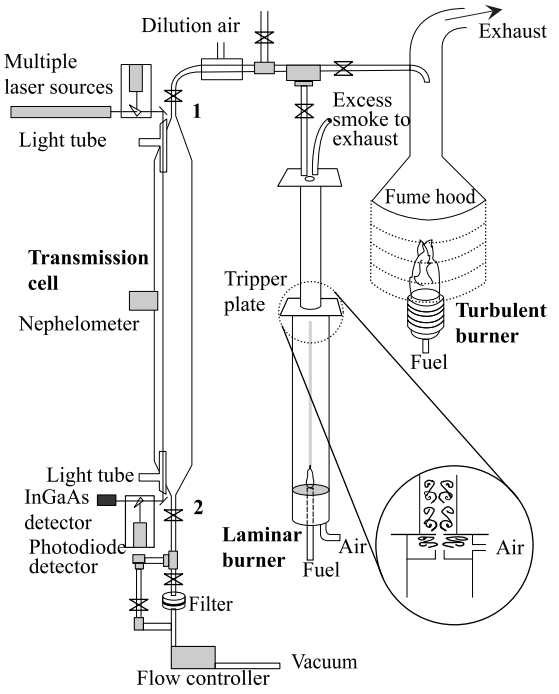

FIGURE 12-27
Large Agglomerate Optics Facility at NIST [180].

transfer in sooty flames. For another, soot is a pollutant and various nonintrusive optical (i.e., radiative) experiments have been designed for its *in situ* detection, such as transmission, scattering, and emission (via laser-induced incandescence or LII) schemes. A state-of-the art device to measure soot extinction coefficients is shown in Fig. 12-27 [180]. The facility is known as the Large Agglomerate Optics Facility (LAOF) at the National Institute for Standards and Technology (NIST), and it is used to measure extinction coefficients of soot generated by various fuels burning under laminar or turbulent conditions. Soot from the laminar or turbulent burner is collected with minimal disturbance of the flame. The collected soot is diluted with air prior to entering the transmission cell. The soot and gas mixture enters the cell at location 1 and exits at location 2. Several near-monochromatic laser sources are available for transmission measurements. The laser beams pass through air-purged "light tubes" at both end, in order to prevent soot deposition on optical surfaces, and the signal can be collected with a choice of detectors (such as the InGaAs and photodiode detectors indicated in the figure). When steady state is reached the mixture is directed across the filter, and the collected soot is carefully weighed after the experiment (with 2–5 μg uncertainty). In addition to extinction measurements the LAOF also collects total scattering data using a reciprocal nephelometer, as also indicated in the figure. The apparatus has been used to measure radiative properties of soot from turbulent acetylene and ethene flames [180], laminar acetylene and ethene flames [181], and turbulent JP-8 combustion [182]

Other measurements of scattering media include properties of titanium dioxide powders, for which Kuhn and coworkers [183] used a loose layer of a powder (20 nm to 3 μm in diameter) supported on a film, while Cabrera and colleagues [184] suspended the TiO_2 particles in water; both used an integrating sphere to capture directional–hemispherical values of the layer's transmissivity and reflectivity. A similar experiment was used by Yaroslavsky *et al.* [185] to capture the radiative properties of biological turbid media. Brewster and Yamada [186] discussed how properties of turbid media can be deduced from time-resolved measurements (using ps pulses), overcoming some of the difficulties of traditional methods; they applied the new scheme to solutions of latex particles.

The measurement of scattered intensity into the near-forward direction poses a unique set of problems, because the signal may vary by several orders of magnitude over a few degrees of scattering angle, and because separating the transmitted radiation from forward scattering is difficult. Although sometimes employed for particle sizing and the determination of the index of refraction, near-forward scattering is of importance primarily in applications with large geometric paths, such as atmospheric scattering, scattering effects on visibility in the seas, astrophysical applications, and so on. In heat transfer applications forward scattering is generally of small importance, since treating it as transmitted radiation usually results in negligible errors. The reader interested in such experiments is referred to the papers by Spinrad and coworkers [187].

References

1. Tien, C. L., and B. L. Drolen: "Thermal radiation in particulate media with dependent and independent scattering," in *Annual Review of Numerical Fluid Mechanics and Heat Transfer*, vol. 1, Hemisphere, New York, pp. 1–32, 1987.
2. Dombrovsky, L. A., and D. Baillis: *Thermal Radiation in Disperse Systems: An Engineering Approach*, Begell House, New York, 2010.
3. van de Hulst, H. C.: *Light Scattering by Small Particles*, John Wiley & Sons, New York, 1957, (also Dover Publications, New York, 1981).
4. Hottel, H. C., A. F. Sarofim, W. H. Dalzell, and I. A. Vasalos: "Optical properties of coatings. Effect of pigment concentration," *AIAA Journal*, vol. 9, pp. 1895–1898, 1971.
5. Brewster, M. Q., and C. L. Tien: "Radiative transfer in packed/fluidized beds: Dependent vs. independent scattering," *ASME Journal of Heat Transfer*, vol. 104, pp. 573–579, 1982.
6. Yamada, Y., J. D. Cartigny, and C. L. Tien: "Radiative transfer with dependent scattering by particles, part 2: Experimental investigation," *ASME Journal of Heat Transfer*, vol. 108, pp. 614–618, 1986.
7. Cartigny, J. D., Y. Yamada, and C. L. Tien: "Radiative transfer with dependent scattering by particles, part 1: Theoretical investigation," *ASME Journal of Heat Transfer*, vol. 108, pp. 608–613, 1986.
8. Drolen, B. L., and C. L. Tien: "Independent and dependent scattering in packed-sphere systems," *Journal of Thermophysics and Heat Transfer*, vol. 1, pp. 63–68, 1987.
9. Drolen, B. L., K. Kumar, and C. L. Tien: "Experiments on dependent scattering of radiation," AIAA paper no. TP-87-210, 1987.
10. Rayleigh, L.: "On the light from the sky, its polarization and colour," *Philos. Mag.*, vol. 41, pp. 107–120, 274–279, 1871, (reprinted in *Scientific Papers by Lord Rayleigh*, vol. I: 1869–1881, No. 8, Dover, New York, 1964).
11. Rayleigh, L.: *Phil. Mag.*, vol. 12, 1881.
12. Lorenz, L.: in *Videnskab Selskab Skrifter*, vol. 6, Copenhagen, Denmark, 1890.
13. Lorenz, L.: in *Oeuvres Scientifiques*, vol. I, Copenhagen, Denmark, p. 405, 1898.
14. Mie, G. A.: "Beiträge zur Optik trüber Medien, speziell kolloidaler Metallösungen," *Annalen der Physik*, vol. 25, pp. 377–445, 1908.
15. Debye, P.: *Annalen der Physik*, vol. 30, no. 4, p. 57, 1909.
16. Kerker, M.: *The Scattering of Light and Other Electromagnetic Radiation*, Academic Press, New York, 1969.
17. Deirmendjian, D.: *Electromagnetic Scattering on Spherical Polydispersions*, Elsevier, New York, 1969.
18. Bohren, C. F., and D. R. Huffman: *Absorption and Scattering of Light by Small Particles*, John Wiley & Sons, New York, 1983.
19. Wylie, C. R.: *Advanced Engineering Mathematics*, 5th ed., McGraw-Hill, New York, 1982.
20. Abramowitz, M., and I. A. Stegun (eds.): *Handbook of Mathematical Functions*, Dover Publications, New York, 1965.
21. Chu, C. M., and S. W. Churchill: "Representation of the angular distribution of radiation scattered by a spherical particle," *Journal of the Optical Society of America*, vol. 45, no. 11, pp. 958–962, 1955.
22. Clark, G. C., C. M. Chu, and S. W. Churchill: "Angular distribution coefficients for radiation scattered by a spherical particle," *Journal of the Optical Society of America*, vol. 47, pp. 81–84, 1957.
23. Kattawar, G. W., and G. N. Plass: "Electromagnetic scattering from absorbing spheres," *Applied Optics*, vol. 6, no. 8, pp. 1377–1383, 1967.
24. Wiscombe, W. J.: "Improved Mie scattering algorithms," *Applied Optics*, vol. 19, pp. 1505–1509, 1980.
25. Modest, M. F., and F. H. Azad: "The influence and treatment of Mie-anisotropic scattering in radiative heat transfer," *ASME Journal of Heat Transfer*, vol. 102, pp. 92–98, 1980.
26. Hodkinson, J. R.: "Light scattering and extinction by irregular particles larger than the wavelength," in *Electromagnetic Scattering*, ed. M. Kerker, Macmillan, New York, pp. 87–100, 1963.
27. Singh, B. P., and M. Kaviany: "Radiative transfer in packed and fluidized beds: Dependent versus independent scattering," *International Journal of Heat and Mass Transfer*, vol. 34, pp. 2869–2882, 1991.
28. Brewster, M. Q.: "Volume scattering of radiation in packed beds of large, opaque spheres," *ASME Journal of Heat Transfer*, vol. 126, no. 4, pp. 1048–1050, 2004.

29. Randrianalisoa, J., and D. Baillis: "Radiative properties of densely packed spheres in semitransparent media: A new geometric optics approach," *Journal of Quantitative Spectroscopy and Radiative Transfer*, vol. 111, no. 10, pp. 1372–1388, 2010.
30. Lee, S. C.: "Radiation heat-transfer model for fibers oriented parallel to diffuse boundaries," *Journal of Thermophysics and Heat Transfer*, vol. 2, no. 4, pp. 303–308, Oct 1988.
31. Tong, T. W., and C. L. Tien: "Analytical models for thermal radiation in fibrous insulation," *Journal of Thermal Insulation*, vol. 4, pp. 27–44, 1980.
32. Tong, T. W., and C. L. Tien: "Radiative heat transfer in fibrous insulations—Part I: Analytical study," *ASME Journal of Heat Transfer*, vol. 105, pp. 70–74, 1983.
33. Tong, T. W., P. S. Swathi, and G. R. Cunnington: "Reduction of radiative heat transfer in thermal insulations by use of dielectric coated fibers," *International Communications in Heat and Mass Transfer*, vol. 16, pp. 851–860, 1989.
34. Swathi, P. S., T. W. Tong, and G. R. Cunnington: "Scattering of electromagnetic waves by cylinders coated with a radially-inhomogeneous layer," *Journal of Quantitative Spectroscopy and Radiative Transfer*, vol. 46, no. 4, pp. 281–292, 1991.
35. Cunnington, G. R., T. W. Tong, and P. S. Swathi: "Angular scattering of radiation from coated cylindrical fibers," *Journal of Quantitative Spectroscopy and Radiative Transfer*, vol. 48, no. 4, pp. 353–362, 1992.
36. Tong, T. W., and W. Li: "Enhancement of thermal emission from porous radiant burners," *Journal of Quantitative Spectroscopy and Radiative Transfer*, vol. 53, no. 2, pp. 235–248, 1995.
37. Lee, S. C.: "Radiative transfer through a fibrous medium: Allowance for fiber orientation," *Journal of Quantitative Spectroscopy and Radiative Transfer*, vol. 36, no. 3, pp. 253–263, 1986.
38. Lee, S. C.: "Effect of fiber orientation on thermal radiation in fibrous media," *International Journal of Heat and Mass Transfer*, vol. 32, no. 2, pp. 311–320, 1989.
39. Lee, S. C.: "Scattering phase function for fibrous media," *International Journal of Heat and Mass Transfer*, vol. 33, no. 10, pp. 2183–2190, 1990.
40. Lee, S. C.: "Dependent scattering of an obliquely incident plane wave by a collection of parallel cylinders," *Journal of Applied Physics*, vol. 68, no. 10, pp. 4952–4957, 1990.
41. Lee, S. C.: "Dependent scattering by parallel fibers: Effects of multiple scattering and wave interference," *Journal of Thermophysics and Heat Transfer*, vol. 6, no. 4, pp. 589–595, 1992.
42. Lee, S. C.: "Angle of incidence and size effects on dependent scattering in fibrous media," *ASME Journal of Heat Transfer*, vol. 118, no. 4, pp. 931–936, 1996.
43. Cunnington, G. R., S. C. Lee, and S. M. White: "Radiative properties of fiber-reinforced aerogel: Theory versus experiment," *Journal of Thermophysics and Heat Transfer*, vol. 12, no. 1, pp. 17–22, 1998.
44. Kumar, S., and S. M. White: "Dependent scattering properties of woven fibrous insulations for normal incidence," *ASME Journal of Heat Transfer*, vol. 117, no. 1, pp. 160–166, 1995.
45. Dombrovsky, L. A.: "Quartz–fiber thermal insulation: Infrared radiative properties and calculation of radiative–conductive heat transfer," *ASME Journal of Heat Transfer*, vol. 118, no. 2, pp. 408–414, 1996.
46. Marschall, J., and F. S. Milos: "The calculation of anisotropic extinction coefficients for radiation diffusion in rigid fibrous ceramic insulations," *International Journal of Heat and Mass Transfer*, vol. 40, pp. 627–634, 1997.
47. Yamada, J., and Y. Kurosaki: "Radiative characteristics of fibers with a large size parameter," *International Journal of Heat and Mass Transfer*, vol. 43, no. 6, pp. 981–991, 2000.
48. van de Hulst, H. C.: "Asymptotic fitting, a method for solving anisotropic transfer problems in thick layers," *Journal of Computational Physics*, vol. 3, pp. 291–306, 1968.
49. Hansen, J. E.: "Exact and approximate solutions for multiple scattering by cloudy and hazy planetary atmospheres," *Journal of the Atmospheric Sciences*, vol. 26, pp. 478–487, 1969.
50. Potter, J. F.: "The delta function approximation in radiative transfer theory," *Journal of the Atmospheric Sciences*, vol. 27, pp. 943–949, 1970.
51. Joseph, J. H., W. J. Wiscombe, and J. A. Weinman: "The delta-Eddington approximation for radiative flux transfer," *Journal of the Atmospheric Sciences*, vol. 33, pp. 2452–2459, 1976.
52. Crosbie, A. L., and G. W. Davidson: "Dirac-delta function approximations to the scattering phase function," *Journal of Quantitative Spectroscopy and Radiative Transfer*, vol. 33, no. 4, pp. 391–409, 1985.
53. Davies, R.: "Fast azimuthally dependent model of the reflection of solar radiation by plane-parallel clouds," *Applied Optics*, vol. 19, pp. 250–255, 1980.
54. Mishchenko, M. I.: "Electromagnetic scattering by nonspherical particles: A tutorial review," *Journal of Quantitative Spectroscopy and Radiative Transfer*, vol. 110, no. 11, pp. 808–832, 2009.
55. Wriedt, T.: "Light scattering theories and computer codes," *Journal of Quantitative Spectroscopy and Radiative Transfer*, vol. 110, no. 11, pp. 833–843, 2009.
56. Waterman, P. C.: "Matrix formulation fo electromagnetic scattering," *Proceedings of IEEE*, vol. 53(8), p. 805, 1965.
57. Mishchenko, M. I., L. D. Travis, and D. W. Mackowski: "*T*-matrix computations of light scattering by nonspherical particles: A review," *Journal of Quantitative Spectroscopy and Radiative Transfer*, vol. 55, no. 5, pp. 535–575, 1996.
58. Mackowski, D. W.: "Calculation of total cross sections of multi-sphere clusters," *Journal of the Optical Society of America*, vol. 11, pp. 2851–2861, 1994.
59. Liu, L., and M. I. Mishchenko: "Scattering and radiative properties of complex soot and soot-containing aggregate particles," *Journal of Quantitative Spectroscopy and Radiative Transfer*, vol. 106, pp. 262–273, 2007.

60. Mishchenko, M. I., N. T. Zakharova, G. Videen, N. G. Khlebtsov, and T. Wriedt: "Comprehensive T-matrix reference database: A 2007–2009 update," *Journal of Quantitative Spectroscopy and Radiative Transfer*, vol. 111, pp. 650–658, 2010.
61. Zhao, Y., and L. Ma: "Assessment of two fractal scattering models for the prediction of the optical characteristics of soot aggregates," *Journal of Quantitative Spectroscopy and Radiative Transfer*, vol. 110, no. 4-5, pp. 315–322, 2009.
62. Yin, J. Y., and L. H. Liu: "Influence of complex component and particle polydispersity on radiative properties of soot aggregate in atmosphere," *Journal of Quantitative Spectroscopy and Radiative Transfer*, vol. 111, no. 14, pp. 2115–2126, 2008.
63. Mishchenko, M. I., L. D. Travis, and D. W. Mackowski: *T-Matrix Codes for Computing Electromagnetic Scattering by Nonspherical and Aggregated Particles* available from http://www.giss.nasa.gov/staff/mmishchenko/t_matrix.html.
64. Wriedt, T.: *SCATTPORT* available from http://www.scattport.org/.
65. Xu, Y.-L.: "Scattering Mueller matrix of an ensemble of variously shaped small particles," *Journal of the Optical Society of America*, vol. 20, no. 11, pp. 2093–2105, 2003.
66. Xu, Y.-L., and N. G. Khlebtsov: "Orientational-averaged radiative properties of an arbitrary configuration of scatterers," *Journal of Quantitative Spectroscopy and Radiative Transfer*, vol. 79–80, pp. 1121–1137, 2003.
67. Xu, Y.-L.: "Electromagnetic scattering by an aggregate of spheres," *Applied Optics*, vol. 34, pp. 4573–4588, 1995.
68. Xu, Y.-L.: "Electromagnetic scattering by an aggregate of spheres: Far field," *Applied Optics*, vol. 36, pp. 9496–9508, 1995.
69. Liu, F., and G. J. Smallwood: "Effect of aggregation on the absorption cross-section of fractal soot aggregates and its impact on LII modelling," *Journal of Quantitative Spectroscopy and Radiative Transfer*, vol. 111, no. 2, pp. 302–308, 2010.
70. Liu, F., and G. J. Smallwood: "Radiative properties of numerically generated fractal soot aggregates: The importance of configuration averaging," *ASME Journal of Heat Transfer*, vol. 132, no. 1, p. 023308, 2010.
71. Li, H., C. Liu, L. Bi, P. Yang, and G. W. Kattawar: "Numerical accuracy of "equivalent" spherical approximations for computing ensemble-averaged scattering properties of fractal soot aggregates," *Journal of Quantitative Spectroscopy and Radiative Transfer*, vol. 111, no. 14, pp. 2127–2132, 2008.
72. Xu, Y.-L.: *Generalized Multi-Sphere Mie Solution Programs* available from http://www.scattport.org-/files/xu/codes.htm.
73. Purcell, E. M., and C. R. Pennypecker: "Scattering and absorption by non-spherical dielectric grains," *Astrophysical Journal*, vol. 186, pp. 705–714, 1973.
74. Mulholland, G. W., C. F. Bohren, and K. A. Fuller: "Light scattering by agglomerates: Coupled electric and magnetic dipole method," *Langmuir*, vol. 10, pp. 2533–2546, 1994.
75. Mulholland, G. W., and R. D. Mountain: "Coupled dipole calculation of extinction coefficient and polarization ratio for smoke agglomerates," *Combustion and Flame*, vol. 119, pp. 56–68, 1999.
76. Sarofim, A. F., and H. C. Hottel: "Radiative transfer in combustion chambers: Influence of alternative fuels," in *Proceedings of the Sixth International Heat Transfer Conference*, vol. 6, Hemisphere, Washington, D.C., pp. 199–217, 1978.
77. Foster, P. J., and C. R. Howarth: "Optical constants of carbons and coals in the infrared," *Carbon*, vol. 6, pp. 719–729, 1968.
78. Blokh, A. G.: "The problem of flame as a disperse system," in *Heat Transfer in Flames*, eds. N. F. Afghan and J. M. Beer, Scripta Book Co., Washington, pp. 111–130, 1974.
79. Blokh, A. G., and L. D. Burak: "Primary radiation characteristics of solid fuels," *Thermal Engineering*, vol. 20, no. 8, pp. 65–70, 1973.
80. Lowe, A., I. M. Stewart, and T. F. Wall: "The measurement and interpretation of radiation from fly-ash particles in large pulverized coal flames," in *Seventeenth Symposium (International) on Combustion*, The Combustion Institute, pp. 105–114, 1979.
81. Blokh, A. G., Sagadeev, and V. D. Vyushin: "Experimental and theoretical investigation of radiation properties of flame with coal burning in powerful boiler furnaces," in *Heat and Mass Transfer-VI*, vol. VIII, Soviet Academy of Sciences (in Russian), Minsk, pp. 70–73, 1980.
82. Wall, T. F., A. Lowe, L. J. Wibberley, T. Mai-Viet, and R. P. Gupta: "Fly-ash characteristics and radiative heat transfer in pulverized-coal-fired furnaces," *Combustion Science and Technology*, vol. 26, pp. 107–121, 1981.
83. Goodwin, D. G.: "Infrared optical constants of coal slags," Technial Report T-255, Stanford University, California, 1986.
84. Viskanta, R., A. Ugnan, and M. P. Mengüç: "Predictions of radiative properties of pulverized coal and fly-ash polydispersions," ASME paper no. 81-HT-24, 1981.
85. Tien, C. L., D. G. Doornink, and D. A. Rafferty: "Attenuation of visible radiation by carbon smokes," *Combustion Science and Technology*, vol. 6, pp. 55–59, 1972.
86. Buckius, R. O., and D. C. Hwang: "Radiation properties for polydispersions: Application to coal," *ASME Journal of Heat Transfer*, vol. 102, pp. 99–103, 1980.
87. Mengüç, M. P., and R. Viskanta: "On the radiative properties of polydispersions: A simplified approach," *Combustion Science and Technology*, vol. 44, pp. 143–159, 1985.
88. Kim, C., and N. Lior: "A simplified model for spectral radiative properties in pulverized coal combustors," in *Heat Transfer in Hazardous Waste Processing*, vol. HTD-212, ASME, pp. 113–122, 1992.

89. Liu, F., and J. Swithenbank: "The effects of particle size distribution and refractive index on fly-ash radiative properties using a simplified approach," *International Journal of Heat and Mass Transfer*, vol. 36, no. 7, pp. 1905–1912, 1993.
90. Im, K. H., and R. K. Ahluwalia: "Radiation properties of coal combustion products," *International Journal of Heat and Mass Transfer*, vol. 36, no. 2, pp. 293–302, 1993.
91. Manickavasagam, S., and M. P. Mengüç: "Effective optical properties of pulverized coal particles determined from FT-IR spectrometer experiments," *Energy and Fuels*, vol. 7, no. 6, pp. 860–869, 1993.
92. Caldas, M., and V. Semião: "Modelling of scattering and absorption coefficients for a polydispersion," *International Journal of Heat and Mass Transfer*, vol. 42, no. 24, pp. 4535–4548, 1999.
93. Singer, J. M., and J. Grumer: "Carbon formation in very rich hydrocarbon–air flames—I: Studies of chemical content, temperature, ionization and particulate matter," in *Seventh Symposium (International) on Combustion*, The Combustion Institute, pp. 559–572, 1959.
94. Wersborg, B. L., J. B. Howard, and G. C. Williams: "Physical mechanisms in carbon formation in flames," in *Fourteenth Symposium (International) on Combustion*, The Combustion Institute, pp. 929–940, 1972.
95. Kunugi, M., and H. Jinno: "Determination of size and concentration of soot particles in diffusion flames by a light-scattering technique," in *Eleventh Symposium (International) on Combustion*, The Combustion Institute, pp. 257–266, 1966.
96. Sato, T., T. Kunitomo, S. Yoshi, and T. Hashimoto: "On the monochromatic distribution of the radiation from the luminous flame," *Bulletin of Japan Society of Mechanical Engineers*, vol. 12, pp. 1135–1143, 1969.
97. Frenklach, M., H. Wang, and M. J. Rabinowitz: "Optimization and analysis of large chemical kinetic mechanisms using the solution mapping method—combustion of methane," *Progress in Energy and Combustion Science*, vol. 18, pp. 47–73, 1992.
98. Frenklach, M., and H. Wang: "Detailed mechanism and modeling of soot particle formation," in *Soot Formation in Combustion*, Springer Verlag, New York, pp. 162–192, 1994.
99. Bockhorn, H.: *Soot Formation in Combustion*, Springer Verlag, New York, 1994.
100. Frenklach, M.: "On surface growth mechanism of soot particles," in *Twenty-Sixth Symposium (International) on Combustion*, The Combustion Institute, pp. 2285–2293, 1996.
101. Kennedy, I. M.: "Models of soot formation and oxidation," *Progress in Energy and Combustion Science*, vol. 23, pp. 95–132, 1997.
102. Wang, H., and M. Frenklach: "A detailed kinetic modeling study of aromatics formation in laminar premixed acetylene and ethylene flames," *Combustion and Flame*, vol. 110, pp. 173–221, 1997.
103. Kazakov, A., and M. Frenklach: "Dynamic modeling of soot particle coagulation and aggregation: Implementation with the method of moments and application to high-pressure laminar premixed flames," *Combustion and Flame*, vol. 114, no. 3-4, pp. 484–501, 1998.
104. Appel, J., H. Bockhorn, and M. Frenklach: "Kinetic modeling of soot formation with detailed chemistry and physics: Laminar premixed flames of C_2 hydrocarbons," *Combustion and Flame*, vol. 121, pp. 122–136, 2000.
105. Richter, H., and J. B. Howard: "Formation of polycyclic aromatic hydrocarbons and their growth to soot – a review of chemical reaction pathways," *Progress in Energy and Combustion Science*, vol. 26, pp. 565–608, 2000.
106. Frenklach, M., and S. J. Harris: "Aerosol dynamics modeling using the method of moments," *J. Coll. Interf. Sci.*, vol. 118, pp. 252–261, 1987.
107. Frenklach, M., and S. J. Harris: "Aerosol dynamics using the method of moments," *J. Coll. Interf. Sci.*, vol. 130, pp. 252–261, 1987.
108. Frenklach, M.: *Soot Modeling Home Page* http://www.me.berkeley.edu/soot.
109. Becker, A.: *Annalen der Physik*, vol. 28, p. 1017, 1909.
110. Millikan, R. C.: "Optical properties of soot," *Journal of the Optical Society of America*, vol. 51, pp. 698–699, 1961.
111. Millikan, R. C.: "Sizes, optical properties and temperatures of soot particles," in *The Fourth Symposium on Temperature, Its Measurement and Control in Science and Industry*, vol. 3, pp. 497–507, 1961.
112. Dalzell, W. H., and A. F. Sarofim: "Optical constants of soot and their application to heat-flux calculations," *ASME Journal of Heat Transfer*, vol. 91, no. 1, pp. 100–104, 1969.
113. Stull, V. R., and G. N. Plass: "Emissivity of dispersed carbon particles," *Journal of the Optical Society of America*, vol. 50, no. 2, pp. 121–129, 1960.
114. Howarth, C. R., P. J. Foster, and M. W. Thring: "The effect of temperature on the extinction of radiation by soot particles," in *Proceedings of the Third International Heat Transfer Conference*, vol. 5, Hemisphere, Washington, D.C., pp. 122–128, 1966.
115. Hubbard, G. L., and C. L. Tien: "Infrared mean absorption coefficients of luminous flames and smoke," *ASME Journal of Heat Transfer*, vol. 100, pp. 235–239, 1978.
116. Medalia, A. I., and L. W. Richards: "Tinting strength of carbon black," *Journal of Colloid and Interface Science*, vol. 40, pp. 233–252, 1972.
117. Graham, S. C.: "The refractive indices of isolated and of aggregated soot particles," *Combustion Science and Technology*, vol. 9, pp. 159–163, 1974.
118. Janzen, J.: "The refractive index of colloidal carbon," *Journal of Colloid and Interface Science*, vol. 69, 1979.
119. Lee, S. C., and C. L. Tien: "Optical constants of soot in hydrocarbon flames," in *Eighteenth Symposium (International) on Combustion*, The Combustion Institute, pp. 1159–1166, 1980.
120. Moss, T. S., G. J. Burrell, and B. Ellis: *Semiconductor Opto-Electronics*, John Wiley & Sons, New York, 1972.

121. Buckius, R. O., and C. L. Tien: "Infrared flame radiation," *International Journal of Heat and Mass Transfer*, vol. 20, pp. 93–106, 1977.
122. Bard, S., and P. J. Pagni: "Carbon particulate in small pool fire flames," *ASME Journal of Heat Transfer*, vol. 103, pp. 357–362, 1981.
123. Chang, H., and T. T. Charalampopoulos: "Determination of the wavelength dependence of refractive indices of flame soot," *Proceedings of the Royal Society (London) A*, vol. 430, no. 1880, pp. 577–591, 1990.
124. Köylü, Ü. Ö., and G. M. Faeth: "Spectral extinction coefficients of soot aggregates from turbulent diffusion flames," *ASME Journal of Heat Transfer*, vol. 118, pp. 415–421, 1996.
125. Felske, J. D., T. T. Charalampopoulos, and H. S. Hura: "Determination of refractive indices of soot particles from the reflectivities of compressed soot particles," *Combustion Science and Technology*, vol. 37, pp. 263–284, 1984.
126. Jones, A. R.: "An estimate of the possible effects of particle agglomeration on the emissivity of sooty flames," in *Combustion Institute European Symposium*, pp. 376–381, 1973.
127. Lee, S. C., and C. L. Tien: "Effect of soot shape on soot radiation," *Journal of Quantitative Spectroscopy and Radiative Transfer*, vol. 29, pp. 259–265, 1983.
128. Mackowski, D. W., R. A. Altenkirch, and M. P. Mengüç: "Extinction and absorption coefficients of cylindrically-shaped soot particles," *Combustion Science and Technology*, vol. 40, pp. 399–410, 1987.
129. Dobbins, R. A., and C. M. Megaridis: "Morphology of flame-generated soot as determined by thermophoretic sampling," *Langmuir*, vol. 3, pp. 254–259, 1987.
130. Samson, R. J., G. W. Mulholland, and J. W. Gentry: "Structural analysis of soot agglomerates," *Langmuir*, vol. 3, pp. 272–281, 1987.
131. Jullien, R., and R. Botet: *Aggregation and Fractal Aggregates*, World Scientific Publishing Co., Singapore, 1987.
132. Köylü, Ü. Ö., and G. M. Faeth: "Structure of overfire soot in buoyant turbulent diffusion flames at long residence times," *Combustion and Flame*, vol. 89, pp. 140–156, 1992.
133. Farias, T. L., M. G. Carvalho, and Ü. Ö. Köylü: "Radiative heat transfer in soot-containing combustion systems with aggregation," *International Journal of Heat and Mass Transfer*, vol. 41, no. 17, pp. 2581–2587, 1998.
134. Hu, B., B. Yang, and Ü. Ö. Köylü: "Soot measurements at the axis of an ethylene/air nonpremixed turbulent jet flame," *Combustion and Flame*, vol. 134, pp. 93–106, 2003.
135. Chakrabarty, R. K., H. Moosmller, W. P. Arnott, M. A. Garro, J. G. Slowik, E. S. Cross, J.-H. Han, P. Davidovits, T. B. Onasch, and D. R. Worsnop: "Light scattering and absorption by fractal-like carbonaceous chain aggregates: Comparison of theories and experiment," *Applied Optics*, vol. 86, pp. 6990–7006, 2007.
136. Sorensen, C. M., and G. C. Roberts: "The prefactor of fractal aggregates," *Journal of Colloid and Interface Science*, vol. 186, pp. 447–452, 1997.
137. Kumar, S., and C. L. Tien: "Effective diameter of agglomerates for radiative extinction and scattering," *Combustion Science and Technology*, no. 66, pp. 199–216, 1989.
138. Ku, J. C., and K. H. Shim: "Optical diagnostics and radiative properties of simulated soot agglomerates," *ASME Journal of Heat Transfer*, vol. 113, no. 4, pp. 953–958, 1991.
139. Ku, J. C., and K. H. Shim: "A comparison of solutions for light scattering and absorption by agglomerated or arbitrarily-shaped particles," *Journal of Quantitative Spectroscopy and Radiative Transfer*, vol. 47, pp. 201–220, 1992.
140. Charalampopoulos, T. T., and P. K. Panigrahi: "Depolarization characteristics of agglomerated particulates-reciprocity relations," *Journal of Physics D: Applied Physics*, vol. 26, pp. 2075–2081, 1993.
141. Lou, W., and T. T. Charalampopoulos: "On the electromagnetic scattering and absorption of agglomerated small spherical particles," *Journal of Physics D: Applied Physics*, vol. 27, pp. 2258–2270, 1994.
142. Lou, W., and T. T. Charalampopoulos: "On the inverse scattering problem for characterization of agglomerated particulates: Partial derivative formulation," *Journal of Physics D: Applied Physics*, vol. 28, pp. 2585–2594, 1995.
143. Mengüç, M. P., A. Mahadeviah, K. Saito, and S. Manickavasagam: "Application of the discrete dipole approximation to determine the radiative properties of soot agglomerates," in *Heat Transfer in Fire and Combustions Systems*, eds. A. M. Kanury and M. Q. Brewster, vol. HTD-199, ASME, pp. 9–16, 1992.
144. Vaglieco, B. M., O. Monda, F. E. Corcione, and M. P. Mengüç: "Optical and radiative properties of particulates at Diesel engine exhaust," *Combustion Science and Technology*, vol. 102, pp. 283–299, 1994.
145. Ivezić, Ž., and M. P. Mengüç: "An investigation of dependent/independent scattering regimes using a discrete dipole approximation," *International Journal of Heat and Mass Transfer*, vol. 39, no. 4, pp. 811–822, 1996.
146. Ivezić, Ž., M. P. Mengüç, and T. G. Knauer: "A procedure to determine the onset of soot agglomeration from multi-wavelength experiments," *Journal of Quantitative Spectroscopy and Radiative Transfer*, vol. 57, no. 6, pp. 859–865, 1997.
147. Nelson, J.: "Test of a mean field theory for the optics of fractal clusters," *J. Modern Optics*, vol. 36, pp. 1031–1057, 1989.
148. Chen, H. Y., M. F. Iskander, and J. E. Penner: "Light scattering and absorption by fractal agglomerates and coagulations of smoke aerosols," *Journal of Modern Optics*, vol. 2, pp. 171–181, 1990.
149. Chen, H. Y., M. F. Iskander, and J. E. Penner: "Empirical formula for optical absorption by fractal aerosol aggregates," *Applied Optics*, vol. 30, pp. 1547–1551, 1991.
150. Dobbins, R. A., and C. M. Megaridis: "Absorption and scattering light by polydisperse aggregates," *Applied Optics*, vol. 30, pp. 4747–4754, 1991.
151. Köylü, Ü. Ö., and G. M. Faeth: "Radiative properties of flame-generated soot," *ASME Journal of Heat Transfer*, vol. 115, no. 2, pp. 409–417, 1993.

152. Farias, T. L., M. G. Carvalho, Ü. Ö. Köylü, and G. M. Faeth: "Computational evaluation of approximate Rayleigh–Debye–Gans fractal-aggregate theory for the absorption and scattering properties of soot," *ASME Journal of Heat Transfer*, vol. 117, no. 1, pp. 152–159, 1995.
153. Farias, T. L., M. G. Carvalho, and Ü. Ö. Köylü: "The range of validity of the Rayleigh–Debye–Gans theory for optics of fractal aggregates," *Applied Optics*, vol. 35, pp. 6560–6567, 1996.
154. Manickavasagam, S., and M. P. Mengüç: "Scattering matrix elements of fractal-like soot agglomerates," *Journal of Applied Physics*, vol. 36, no. 6, pp. 1337–1351, 1997.
155. Krishnan, S. S., K. C. Lin, and G. M. Faeth: "Spectral extinction coefficients of soot aggregates from turbulent diffusion flames," *ASME Journal of Heat Transfer*, vol. 123, pp. 331–339, 2001.
156. Jones, A. R.: "Electromagnetic wave scattering by assemblies of particles in the Rayleigh approximation," *Proceedings of the Royal Society (London) A*, vol. 366, pp. 111–127, 1979.
157. Jones, A. R.: "Scattering efficiency factors for agglomerates of small spheres," *Journal of Physics D: Applied Physics*, vol. 12, pp. 1661–1672, 1979.
158. Saxon, D. S.: Technical Report CRI 40816, NASA, 1973.
159. Iskander, M. F., H. Y. Chen, and J. E. Penner: "Optical scattering and absorption by branched-chains of aerosols," *Applied Optics*, vol. 28, pp. 3083–3091, 1989.
160. Mackowski, D. W., and M. I. Mishchenko: "Calculation of the T matrix and the scattering matrix for ensembles of spheres," *Journal of the Optical Society of America*, vol. 13, no. 11, pp. 2266–2278, 1996.
161. Liu, L., M. I. Mishchenko, and W. P. Arnott: "A study of radiative properties of fractal soot aggregates using the superposition T-matrix method," *Journal of Quantitative Spectroscopy and Radiative Transfer*, vol. 109, no. 15, pp. 2656–2663, 2008.
162. Sorensen, C. M.: "Light scattering by fractal aggregates: A review," *Aerosol Science and Technology*, vol. 35, pp. 648–687, 2001.
163. Köylü, Ü. Ö., and G. M. Faeth: "Optical properties of overfire soot in buoyant turbulent diffusion flames at long residence times," *ASME Journal of Heat Transfer*, vol. 116, no. 1, pp. 152–159, 1994.
164. Mackowski, D. W.: "A simplified model to predict the effects of aggregation on the absorption properties of soot particles," *Journal of Quantitative Spectroscopy and Radiative Transfer*, vol. 100, pp. 237–249, 2006.
165. Köylü, Ü. Ö., C. S. McEnally, D. E. Rosner, and L. D. Pfefferle: "Simultaneous measurements of soot volume fraction and particle size/microstructure in flames using a thermophoretic sampling technique," *Combustion and Flame*, vol. 110, pp. 494–507, 1997.
166. Felske, J. D., and C. L. Tien: "The use of the Milne–Eddington absorption coefficient for radiative heat transfer in combustion systems," *ASME Journal of Heat Transfer*, vol. 99, no. 3, pp. 458–465, 1977.
167. Agarwal, B. M., and M. P. Mengüç: "Forward and inverse analysis of single and multiple scattering of collimated radiation in an axisymmetric system," *International Journal of Heat and Mass Transfer*, vol. 34, no. 3, pp. 633–647, 1991.
168. Bryant, F. D., B. A. Sieber, and P. Latimer: "Absolute optical cross sections of cells and chloroplasts," *Arch. Biochem. Biophys.*, vol. 135, pp. 97–108, 1969.
169. Roessler, D. M., and F. R. Faxvog: "Optoacoustic measurement of optical absorption in acetylene smoke," *Journal of the Optical Society of America*, vol. 69, pp. 1699–1704, 1979.
170. Faxvog, F. R., and D. M. Roessler: "Optoacoustic measurement of Diesel particulate emission," *Journal of Applied Physics*, vol. 50, pp. 7880–7882, 1979.
171. Härd, S., and O. Nilsson: "Laser heterodyne apparatus for measuring small angle scattering from particles," *Applied Optics*, vol. 18, pp. 3018–3026, 1979.
172. Hottel, H. C., A. F. Sarofim, I. A. Vasalos, and W. H. Dalzell: "Multiple scatter: Comparison of theory with experiment," *ASME Journal of Heat Transfer*, vol. 92, pp. 285–291, 1970.
173. Menart, J. A., H. S. Lee, and R. O. Buckius: "Experimental determination of radiative properties for scattering particulates," *Experimental Heat Transfer*, vol. 2, no. 4, p. 309, 1989.
174. Woodward, D. H.: "He-Ne laser as source for light scattering measurements," *Applied Optics*, vol. 2, pp. 1205–1207, 1963.
175. Woodward, D. H.: "Multiple light scattering by spherical dielectric particles," *Journal of the Optical Society of America*, vol. 54, pp. 1325–1331, 1964.
176. Hartel, W.: "Zur Theorie der Lichstreuung durch trübe Schichten, besonders Trübgläser," *Licht*, vol. 10, pp. 141–143, 232–234, 1940.
177. Smart, C., R. Jacobsen, M. Kerker, P. Kratohvil, and E. Matijevic: "Experimental study of multiple light scattering," *Journal of the Optical Society of America*, vol. 55, no. 8, pp. 947–955, 1965.
178. Orchard, S. E.: "Multiple scattering by spherical dielectric particles," *Journal of the Optical Society of America*, vol. 55, pp. 737–738, 1965.
179. Daniel, K. J., N. M. Laurendeau, and F. P. Incropera: "Optical property measurements for suspensions of unicellular algae," ASME paper no. 78-HT-14, 1978.
180. Mulholland, G. W., and M. Y. Choi: "Measurement of the mass specific extinction coefficient for acetylene and ethene smoke using the large agglomerate optics facility," *Proceedings of the Combustion Institute*, vol. 27, pp. 1515–1522, 1998.
181. Zhu, J. Y., M. Y. Choi, G. W. Mulholland, S. L. Manzello, L. A. Gritzo, and J. Suo-Anttila: "Measurement of visible and near-ir optical properties of soot produced from laminar flames," *Proceedings of the Combustion Institute*, vol. 29, pp. 2367–2374, 2003.

182. Zhu, J. Y., A. Irrera, M. Y. Choi, G. W. Mulholland, J. Suo-Anttila, and L. A. Gritzo: "Measurement of light extinction constant of JP-8 soot in the visible and near-infrared spectrum," *International Journal of Heat and Mass Transfer*, vol. 47, no. 17–18, pp. 3643–3648, 2004.
183. Kuhn, J., S. Korder, and M. C. Arduini-Schuster: "Infrared-optical transmission and reflection measurements on loose powders," *Review of Scientific Instruments*, vol. 64, pp. 2523–2530, 1993.
184. Cabrera, M. I., O. M. Alfano, and A. E. Cassano: "Absorption and scattering coefficients of titanium dioxide particulate suspensions in water," *Journal of Physical Chemistry*, vol. 100, pp. 20043–20050, 1996.
185. Yaroslavsky, I. V., A. N. Yaroslavsky, and T. Goldbach: "Inverse hybrid technique for determining the optical properties of turbid media from integrating-sphere measurements," *Applied Optics*, vol. 35, pp. 6797–6809, 1996.
186. Brewster, M. Q., and Y. Yamada: "Optical properties of thick, turbid media from picosecond time-resolved light scattering measurements," *International Journal of Heat and Mass Transfer*, vol. 38, no. 14, pp. 2569–2581, 1995.
187. Spinrad, R. W., J. R. V. Zaneveld, and H. Pak: "Volume scattering function of suspended particulate matter at near-forward angles: A comparison of experimental and theoretical values," *Applied Optics*, vol. 17, no. 7, pp. 1125–1130, 1978.

Problems

12.1 A mass of m (kg) of coal is ground into particles of equal size a (μm), which may be assumed to be "large" and black. Determine the optical thickness (based on radius R) of the resulting spherical particle cloud, assuming that the particles are uniformly distributed throughout the volume.

12.2 One way to determine the number of particles in a gas is to measure the absorption coefficient for the cloud. For a cloud of large, diffuse particles ($x \gg 1$, $\epsilon_\lambda = 0.4$), the particle distribution function is known to be of the form

$$n(a) = \begin{cases} C = \text{const}, & 100\,\mu\text{m} < a < 500\,\mu\text{m}, \\ 0, & \text{elsewhere.} \end{cases}$$

If κ_λ is measured as $1\,\text{cm}^{-1}$, determine C and the total number of particles per cm^3.

12.3 Coal particles (gray and diffuse with $\epsilon = 0.9$, $m = 1.925{-}0.1i$) are burnt in a long cylindrical combustion chamber. The combustor is well stirred, resulting in a uniform distribution of particles with a size distribution of

$$n(a) = \begin{cases} 1.5 \times 10^8\ \text{m}^{-4}, & a_{\min} = 1\,\text{mm} < a < a_{\max} = 3\,\text{mm}, \\ 0, & \text{otherwise.} \end{cases}$$

Determine the absorption and scattering coefficients of this particle cloud.

12.4 Consider a particle cloud of fixed-size particles (radius a) contained between parallel plates $0 \le x \le L = 1\,\text{m}$. The volume fraction of particles is $f_v(x) = f_0 + \Delta f\,(x/L)$, and their temperature is $T(x) = T_0 + \Delta T\,(x/L)$, where $\Delta f/f_0 = \Delta T/T_0 = 1$, $f_0 = 1\%$, $T_0 = 500\,\text{K}$. Assuming the particle size to be $a = 500\,\mu$m, and made of a material with a gray hemispherical emittance of $\epsilon_\lambda = 0.7$, show that the large-particle approximation may be used for the infrared. Calculate the local, spectral absorption and scattering coefficients. Determine the local Planck-mean extinction coefficient as well as the total optical thickness of the slab (based on the Planck-mean).

12.5 Black spheres of radius $a = 10\,\mu$m occupy a semi-infinite space with varying number density $N_T = N_0 e^{-z/L}$ ($N_0 = 10^4/\text{cm}^3$, $L = 1$ m). If a HeNe laser ($\lambda = 0.633\mu$m) shines onto this layer (at $z = 0$ into the z-direction), what fraction of its energy is directly transmitted?

12.6 Pulverized coal is burned in a combustor. In order to achieve maximum radiative heat transfer rates, it is desired to keep the optical thickness of the particle cloud at intermediate levels, say $\tau_L = \kappa L = 1$, in the intermediate infrared, or $\lambda = 5\,\mu$m, where $L = 1\,\text{m}$ is a characteristic combustor dimension. Determine the necessary volume fraction of coal dust, if its size distribution may be taken as

$$n(a) \propto \begin{cases} a^{-3}, & 100\,\mu\text{m} \le a \le 1000\,\mu\text{m}, \\ 0, & \text{all other } a. \end{cases}$$

The spectral, hemispherical emittance of coal at $\lambda = 5\,\mu$m is $\epsilon_\lambda = 0.7$.

12.7 To maximize radiative heat loss from a hot medium it is usually desirable for the medium to have an intermediate optical thickness. A nonparticipating hot gas at 1000 K occupying the 1 m wide space

between two parallel plates is to be seeded with platinum particles to make the optical thickness of the slab (based on extinction) unity ($\tau_L = 1.0$). For this purpose a total of $2\,\mathrm{kg/m^3}$ particles are to be used (density of platinum $\simeq 20\,\mathrm{g/cm^3}$).

(a) To what particle radius must the platinum be ground in order to achieve the desired result?

(b) Instead, if platinum spheres of radii 50 μm and 100 μm are available, how much of each (for a total of $2\,\mathrm{kg/m^3}$) must be used to achieve the same result?

12.8 The distribution function of a particle cloud may be approximated by an exponential function such as $n(a) = Ca^2\,e^{-ba}$, where a is particle radius and b and C are constants. It is proposed to determine the distribution function of a set of particles by suspending a measured mass of particles between parallel plates, followed by measuring extinction across the particle layer. Given that $m'' = 0.05\,\mathrm{g/cm^2}$ of particles are present between the plates, which are 10 cm apart, and that the optical thickness based on extinction has been measured as $\tau_0 = 2$:

(*a*) Determine the distribution function above (i.e., b and C).

(*b*) If a single particle size were to be used to achieve the same extinction with the same mass of particles, what would the particle radius be?

You may assume all particles to be "large" and diffuse spheres with an emittance of 0.7 and a density of $\rho = 2\,\mathrm{g/cm^3}$.

12.9 Consider a particle cloud with a distribution function of $n(a) = Ca^2\,e^{-ba}$, where a is particle radius and b and C are constants. The particles are coal ($\epsilon = 1$), and measurements show the particles occupy a volume fraction of 1%, while the number density has been measured as $N_T = 10^6/\mathrm{cm^3}$. Calculate the extinction, absorption, and scattering coefficients of the cloud for the wavelength range $1\,\mu\mathrm{m} < \lambda < 4\,\mu\mathrm{m}$.

12.10 A LIDAR laser beam (operating in the green at $\lambda = 0.6\,\mu$m) is shot into the sky. At a height of 1 km the laser encounters a 200 m thick cloud consisting of water droplets of varying size ($100\,\mu\mathrm{m} \le a \le 200\,\mu\mathrm{m}$), but constant particle distribution function everywhere ($n = 500/\mu\mathrm{m\,m^3}$). What fraction of the laser beam will be transmitted through the cloud? How much will be absorbed? Very approximately, how much would you expect to get scattered back to the Earth's surface? **Carefully** justify your statements about absorption and scattering, using estimates, graphs, and/or physical arguments for support. Qualitatively, how would your explanation change, if you take into account that $k = 10^{-7}$ (i.e., droplets are **not** opaque)?
Note: Water at 0.6 μm has an index of refraction of $m \simeq 1.35 - 10^{-7}i$. For the sake of this problem you may assume the droplets to be opaque (not really true).

12.11 In a coal-burning plant, pulverized coal is used that is known to have a particle size distribution function of

$$n(a) \propto a^2\,e^{-Aa^6}, \quad A = 3 \times 10^{-11}\,\mu\mathrm{m}^{-6}.$$

The coal may be approximated as diffuse spheres with a gray emittance of $\epsilon = 0.3$. What is the effective minimum size parameter, $x_{\min}$ (i.e., 90% by weight of all particles have a size parameter larger than that)? You may assume a combustion temperature of $\approx 2000\,\mathrm{K}$, i.e., the relevant wavelengths range from about 1 μm to about 10 μm. If the furnace is loaded with 10 kg coal particles per cubic meter, what are the spectral absorption and scattering coefficients? (Density of the coal = $2000\,\mathrm{kg/m^3}$.)

12.12 Consider nitrogen mixed with spherical particles at a rate of 10^8 particles/m^3. The particles have a radius of 300 μm and are diffuse-gray with $\epsilon = 0.5$.

(*a*) Determine the absorption and scattering coefficients, and the scattering phase function.

(*b*) Show how the phase function can be approximated by a Henyey–Greenstein function.

(*c*) Can the Crosbie–Davidson model be used for this mixture?

(*d*) Compare the different versions of the phase function in a Φ *vs.* $\cos\Theta$ plot.

12.13 A semi-infinite space is filled with black spheres. At any given distance, z, away from the plate the particle number density is identical, namely $N_T = 6.3662 \times 10^8\,\mathrm{m^{-3}}$. However, the radius of the suspended spheres diminishes monotonically away from the surface as

$$a = a_0\,e^{-z/L}; \quad a_0 = 10^{-4}\,\mathrm{m}, \quad L = 1\,\mathrm{m}.$$

(*a*) Determine the absorption coefficient as a function of z (you may make the large-particle assumption).

(*b*) Determine the optical coordinate as a function of z. What is the total optical thickness of the semi-infinite space?

12.14 A semi-infinite space is filled with black spheres of uniform radius $a = 100\,\mu$m. The particle number density is maximum adjacent to the surface, and decays exponentially away from the surface according to

$$N_T = N_0 e^{-Cz}; \qquad N_0 = 10^8\,\mathrm{m}^{-3}, \qquad C = \pi\,\mathrm{m}^{-1}.$$

(*a*) Determine the absorption and extinction coefficients as functions of z.

(*b*) Determine the optical coordinate as a function of z. What is the total optical thickness of the semi-infinite space?

12.15 In a combustion chamber radiatively nonparticipating gases are mixed with soot and coal particles. The following is known (per m^3 of mixture):

Soot: uniform particle size, $a_s = 10$ nm, mass = 10^{-3} kg,
complex index of refraction $\dfrac{m^2-1}{m^2+2} = 0.5\lambda^2 - 0.1\lambda i$ (λ in μm).

Coal: uniform particle size, $a_c = 1$ mm, mass = 1 kg, coal is black.

The density of both, coal and soot, is 2,000 kg/m^3.
Determine the spectral absorption coefficient of the mixture for the near infrared.

12.16 In a sheet flame confined between two large parallel plates $-L \le z \le +L = 1$ m soot is generated mainly in the central flame region, leading to a local soot volume fraction of $f_v(z) = f_{v0}[1 - (z/L)^2]$, with $f_{v0} = 1.07 \times 10^{-6}$. The soot is propane soot with a complex index of refraction of $m = 2.21 - 1.23i$.

(*a*) Determine the relevant radiative properties of the mixture, assuming the combustion gases to be nonparticipating.

(*b*) What is the spectral optical thickness of the $2L$ thick layer?

12.17 A laser beam at 633 nm wavelength is probing a 1 m thick layer of gold nanoparticles suspended in air (radius $a = 10$ nm; for gold at 633 nm: $m = 0.47 - 2.83i$). If the exiting laser beam is attenuated by 10% due to absorption and scattering, determine

the number density of gold particles,
(b) their volume fraction.

12.18 A LIDAR laser beam (operating in the green at $\lambda = 0.6\mu$m) is shot into the sky. At a height of 1km the laser encounters a 200m thick cloud consisting of tiny water droplets of varying size (1nm $\le a \le$ 20nm), but constant particle distribution function everywhere ($n = 6 \times 10^{15}$/nm m^3).

(a) Determine the water droplet volume fraction in the cloud.

(b) Determine its spectral absorption coefficient; compare with equation (12.123).

(c) What fraction of the laser beam will be transmitted through the cloud? How much will be absorbed?

Note: Water at 0.6μm has an index of refraction of $m \simeq 1.35 - 10^{-7}i$.

12.19 Redo Problem 12.4 for propane soot with a single mean radius of $a_m = 0.1\,\mu$m in a flame with $f_0 = 10^{-6}$ and $T_0 = 1500$ K. Show that the small particle limit is appropriate for, say, $\lambda > 3\,\mu$m. For hand calculations you may approximate the index of refraction by a single average value (say, at $3\,\mu$m), and the emissive power by Wien's law.

12.20 Redo Problem 12.19 for the case that the soot has agglomerated into mass fractal aggregates of 1000 soot particles each ($D_f = 1.77$ and $k_f = 8.1$).

12.21 Consider a particle cloud with a distribution function of $n(a) = Ca^2 e^{-ba}$, where a is particle radius and b and C are constants. The particles are soot ($m \simeq 1.5 - 0.5i$), and measurements show the soot occupies a volume fraction of 10^{-5}, while the number density has been measured as $N_T = 10^{12}$/cm^3. Calculate the extinction, absorption, and scattering coefficients of the cloud for the wavelength range $1\,\mu\mathrm{m} < \lambda < 4\,\mu\mathrm{m}$.